We are IntechOpen,
the world's leading publisher of
Open Access books
Built by scientists, for scientists

4,800
Open access books available

122,000
International authors and editors

135M
Downloads

Our authors are among the

154
Countries delivered to

TOP 1%
most cited scientists

12.2%
Contributors from top 500 universities

CLARIVATE ANALYTICS
BOOK CITATION INDEX
INDEXED

WEB OF SCIENCE™

Selection of our books indexed in the Book Citation Index
in Web of Science™ Core Collection (BKCI)

Interested in publishing with us?
Contact book.department@intechopen.com

Numbers displayed above are based on latest data collected.
For more information visit www.intechopen.com

Novel Planar Hall Sensor for Biomedical Diagnosing Lab-on-a-Chip

Tran Quang Hung, Dong Young Kim,
B. Parvatheeswara Rao and CheolGi Kim

Additional information is available at the end of the chapter

1. Introduction

Increased proliferation of infectious diseases stresses the need for immediate development of a state of the art lab-on-a-chip with the capabilities of single biomolecular recognition and parallel processing not only to minimize the death rates but also to enhance the protection from rapid spread of epidemics. Though there are several methods for detection of biomolecules, the magnetic bead sensing technique has been promising and versatile due to its increased ease of fabrication in miniature designs and also its scope for rapid, inexpensive, high sensitive and ultrahigh resolution point of care diagnosis of several human diseases; thus, magnetic biosensors and biochips have become the subject of intense research interest in recent times globally.

In the magnetic bead sensing technique, the detection of biofunctionalized magnetic beads is normally carried out by sensors that are embedded underneath the sensing regions and provide a direct electrical readout proportional to the surface density of immobilized magnetic beads. There are several magnetic sensor principles in operation; namely, anisotropic magnetoresistance (AMR) sensors [1-2], giant magnetoresistance (GMR) and spin valve sensors [3–6], magnetic tunnel junctions (MTJ) [6-7], micro-Hall sensors [8], and planar Hall effect (PHE) sensors [9–11]. Common procedure employed for all these sensor principles is that the magnetic immunoassay of biological sample is introduced to the biofunctionalized sensor array followed by washing steps. In order to establish reproducible conditions under these various incubation and washing steps, it is desirable to integrate the sensor in a microfluidic system, which further facilitates a study of real time response of the sensor as a function of fluid flow, sensor bias current and bead concentrations. Moreover, multi-analyte biosensors integrated with microfluidic systems can be made to

perform numerous tasks automatically by way of sensitively and specifically detecting multiple targets from unprocessed sample material, thus creating a compact instrument in the form of ''lab-on-a-chip''.

With the phenomenal success of GMR-spin valve sensors and MTJ sensors in hard disc drives and magnetic memories, they have become an inspiration for testing their use in other areas including that of magnetic biodetection. Obviously, GMR and MTJ sensors take pride in finding themselves as one of the most widely investigated magnetic sensors for bioapplications [12-13]. They are also successful biosensors commercially as they offer high sensitivities, flexible sensor geometries and large bead-to-sensor ratio with well established integrated circuit fabrication technology. However, relatively low signal to noise ratio of these sensors may often leave scope for erroneous detection. The AMR sensors, in turn, offer greater ease of fabrication but the sensitivity of the AMR signal measured along the longitudinal direction is, however, limited by Johnson noise originating from thermal fluctuations at high frequencies, and by temperature drift at low frequencies [1]. However, the flaws associated with longitudinal AMR measurements can be greatly improved by measuring the voltage change in the transverse direction instead, a phenomenon known as the planar Hall effect [14]. It has been shown that by using the PHE, the temperature drift was reduced by at least 4 orders of magnitude, and nano-Tesla sensitivity has been exhibited [15]. In addition, compared with longitudinal AMR signals, PHE signals are more sensitive to local spin configuration and have much lower background voltage as well.

We propose here a planar Hall sensor array in exchange biased multilayer structure and demonstrate the performance of the sensor with the capability of detection of a single magnetic bead. Also, the sensor is further shown to be capable of single biomolecule detection. Following a brief introduction on the need for exploring magnetic sensors, the book chapter describes the principle of magnetic sensing and highlights the merits of planar Hall sensor in terms of field sensitivity and resolution in the second section.

In the experimental parts, the details of the general procedure for fabrication sequence of the sensor, its characterization and microarray integration were described. Subsequently, an account on the theory and experiments of bead detection using planar Hall resistance (PHR) sensor in different multilayer structures and geometries leading to a complete evolution of novel PHR sensors is elaborately presented in the fourth section. Nevertheless, a hybrid AMR-PHR sensor in ring geometry has been identified for optimum sensor performance towards the end of this section.

In the fifth section, apart from a brief description on the magnetic beads and their functionalization, a description of sensor performance and its capability for detection of magnetic beads including a single magnetic bead is given. This section also presents an account on the integration of microarray sensors with the aid of microfluidics for performing biomolecule experiments while showing the possibility of the planar Hall sensor for a sensitive detection of even single biomolecule. And, finally, it concludes the processes involved with a specific mention on future trends to cater the needs of the society in general.

2. Principle of magnetic sensors

The principle of detection employed by the magnetic sensors for magnetic bioassay involves a magnetic transduction mechanism which uses the magnetic micro- or nanoparticles as labels. The biomolecules are commonly detected by attaching them to highly specific magnetic labels that can, upon their binding, produce an observable quantitative electrical signal, as compared to the cumbersome detection of light signal from fluorescent labels. The specificity is traditionally achieved through a biomolecular recognition mechanism, such as antigen-antibody affinity which can be accomplished by label functionalization, as demonstrated in Fig.1.
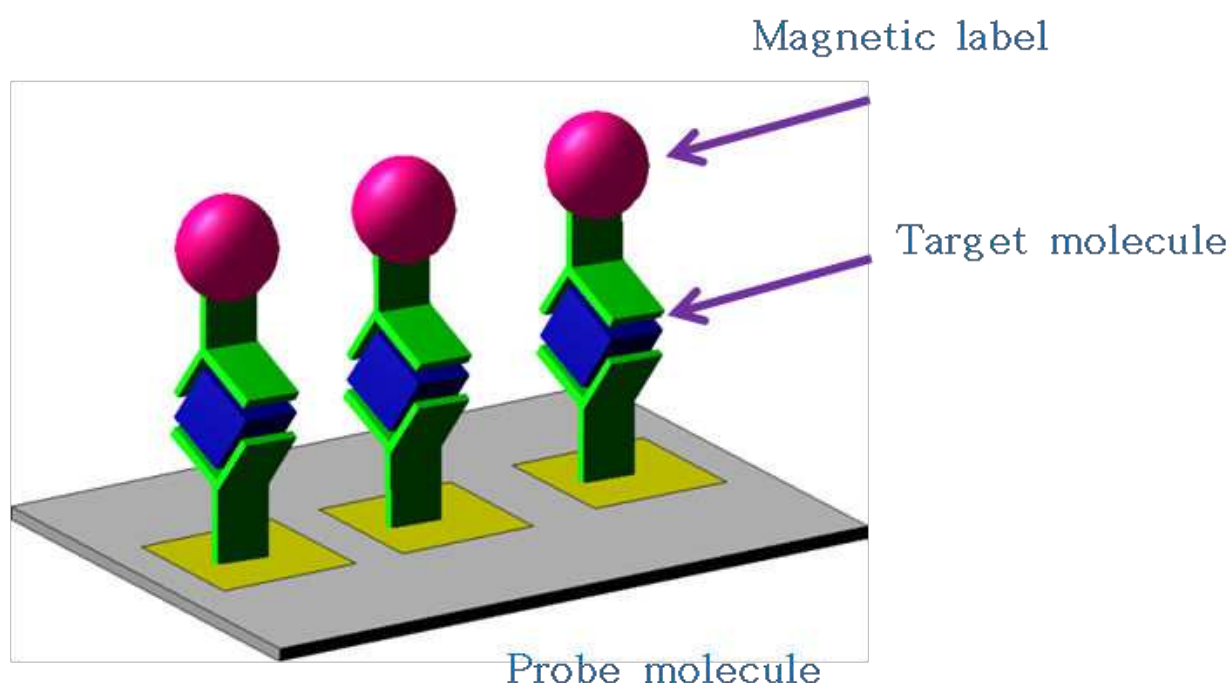
Figure 1. Procedure for the immobilization of probe molecule on the sensor surface and hybridization of the target molecules through Streptavidin coated Dynabeads.

Magnetoresistance (MR) is the property of magnetic materials that results in a change of resistance with applied magnetic field. The MR materials are being developed for the applications such as hard-disk read heads, magnetic random access memories and magnetic field sensors. The materials that display MR property with desired characteristics can replace the inductive coil sensors in a variety of applications including that of biomolecule recognition.

2.1. Magnetoresistive materials for sensing

Thin films and multilayer structures in different geometries show MR characteristics specific to their geometry and all these structures are found to be suitable for one or the other applications. The ferromagnetic single layer exhibits an AMR which is measured in the current

direction, while the planner Hall resistance (PHR) effect can be measured in current perpendicular direction in AMR materials [16]. The AMR and PHR effects are due to the anisotropic magnetoresistivity in ferromagnetic layers. The magnetic thin film multilayer structures can give giant magnetoresistance [17] and tunneling magnetoresistance [18-19] effects and the MR property of these structures are superior to that of the AMR structure. The GMR structure consists of two layers of ferromagnetic metal separated by ultra-thin non-magnetic metal spacer layers. The TMR structures are similar to GMR except that they utilize an ultra-thin insulating layer to separate two magnetic layers rather than a conductor. The GMR and TMR effects occur mainly due to the spin-dependent scattering as the current passes from one layer to the other through the spacer layer. The usual figure of merit of the MR ratio is traditionally defined as

$$
\mathrm{MR}(\%) = \frac{R_{\mathrm{max}} - R_{\mathrm{min}}}{R_{\mathrm{min}}} \times 100 \tag{1}
$$

where R_{max} and R_{min} are the maximum and minimum resistance, respectively. The AMR materials typically have MR ratios about 2 - 6 %, and GMR structures exhibit 10 - 50 % while the TMR structures commonly can achieve over 200 % of MR ratio using MgO tunnel barrier instead of the usual Al_2O_3.

A majority of the studies in MR effect in thin films are devoted to the research of multilayered structures showing the largest possible sensitivity of the resistivity for the magnetic field, and consequently a large number of transition metal-based multilayered structures exhibiting large MR ratios have been found. In connection with the technological problems to be solved, this book chapter devotes to a number of MR sensor designs using the planar Hall effect and tested to linearize the transducer signal, to enhance the resolution limited by the MR ratio.

2.2. Relevant sensor characteristics

Though there is a wide choice for sensor designs, optimum sensor performance in each design can be ensured only when specific sensor characteristics are satisfactorily addressed. Among these characteristics, the field sensitivity and the sensor resolution are of utmost concern particularly for a PHR sensor and, thus, they are considered to be described here for elucidating their importance.

2.2.1. Field sensitivity

The field sensitivity of PHR sensor, *i.e.*, the differential of measured PHR voltage versus applied field, can be obtained as

$$
\frac{\partial V_{\mathrm{PHR}}}{\partial H} = \frac{I(\rho_{//} - \rho_{\perp})}{t} \frac{\cos 2\theta \sin(\gamma - \theta)}{H_{\mathrm{K}} \cos 2\theta + H_{\mathrm{ex}} \cos \theta + H \cos(\gamma - \theta)} \tag{2}
$$

where I is the current passing through the sensing layer, t is the thickness of the ferromagnetic layer, γ is the angle between applied magnetic field and easy axis, H_K is the uniaxial anisotropy field and $\rho_{//}$ and $\rho_{\perp}$ are the resistivity parallel and perpendicular to the magnetization, respectively. In Eq. (2), the field sensitivity depends not only on the intrinsic parameters $\Delta\rho = \rho_{//} - \rho\, H_K$, and exchange bias field (H_{ex}), but also on the extrinsic parameters such as the magnetization angle at an instant applied field, θ, and the applied magnetic field H.

In a typical curve of PHR signal with applied magnetic field, the maximum field sensitivity of PHR sensor is appeared at low (near zero) magnetic fields. Therefore, the PHR sensor can be used as low magnetic field sensors. Also, the PHR signal does not depend on the sensor size such as the width and length, and therefore, the micro or nano meter order of sensor size is possible by maintaining the same output signal. Thus, the PHR sensor is one of the good candidate bio-sensors for the micro- or nano- bead detector.

2.2.2. Resolution (S/N)

A comparative study of the sensor's characteristics was made systematically and summarized in Table 1 for some of the sensors in practice [12]. It must be mentioned that all the compared sensors have similar active areas and were normally designed for detection of single or small number of micro-size particles.

In Table 1, the part (A) represents the dimensions and properties of different sensor devices compared. The represented thickness is that of the sensing volume used in 1/f noise calculations. Whereas the part (B) shows calculated signals obtained from a single 2 μm bead at the center and on the top of the sensor (the center of the bead is 1.2 μm away from the sensing element), when a 15 Oe rms field is applied. Also represented are the 1/f noise and the thermal noise contributions, and the minimum detectable field as calculated from the expressions in the text, and the signal-to-noise ratio under the conditions described in the text.

Sensor type	W (µm)	h (µm)	t^*(nm)	R_{sq}, Ω/RA, Ωµm²	$\Delta R/R$ (%)	H_k (kA/m)	$\Delta R/\Delta(\mu_0 H)$ (V/T A)
(A)							
SV	3	2	10	18	8	2.4	358
PH-AMR	2.5	2.5	20	6.5	3	2.4	32
AMR ring	$R_{int} = 1; R_{ext} = 2$	1	20	6.5	3	2.4	152
GMR	3	2	88	5.3	9	8	71
Hall	2.4	2.4	NA	NA	NA	NA	175
MTJ	2.5	2.5	1	80 (RA)	20 (at 10 mV)	2.4	424

Sensor type	I (mA)	S (µV$_{rms}$)	γ_H, α	N_f (nV$_{rms}$)	N_{therm} (nV$_{rms}$)	$\mu_0 H_{min}$ (nT)	S/N_f
(B)							
SV	10	86	0.1	193	0.61	54	442
PH-AMR	10	15	0.01	10	0.30	32	1453
AMR ring	10	2	0.01	39	0.65	26	50
GMR	5	13	1.2	33	0.33	93	382
Hall	0.3	0.033[a], 4[b]	NA	NA	11	210	3[a], 367[b]
MTJ	1	10	10^{-8} (µm²)	85	0.42	202	114

[a]Particle–sensor separation of 7 µm.
[b]Particle–sensor separation of 1.2 µm.

Table 1. (from ref.12)

The comparison results have shown that the PH-AMR or PHE sensor has prominent advantages over others such as very high signal-to-noise ratio (S/N$_f$) as well as very high resolution ($\mu_o H_{min}$) in the detection of the magnetic field. Furthermore, the voltage profile of a PHE sensor responds linearly to the magnetic field at the small values. This is a prominent advantage in detection of small stray field induced from magnetic labels. Therefore, we have chosen and mainly focused on the development of the PHE sensors for bio-applications.

3. Sensor fabrication and characterization

3.1. Fabrication procedure of a novel planar Hall sensor

Nowadays, with the advancement of the accurate sputtering and lithography technologies, the sensor with desired composition in micro-size can be easily fabricated by using a lift off method. The general fabrication procedure of a novel exchange biased planar Hall sensor, for example in typical spin valve geometry, using the lift off method is shown in a simplified description in the figure 2 below. However, the same procedure is applied for fabrication of other PHR sensors too in different geometries mentioned in this book chapter.

The SiO$_2$ wafer is first cleaned in the acetone and methanol solutions while placing in the ultrasonic bath, then the SiO$_2$ wafer is covered by a commercial photoresist such as Az (5214E, 9260,…) or SU8-(2000, 3000,…) by using a spin coating system with a defined thickness. The blank cross-junctions are stenciled out on the photoresist coated on SiO$_2$ wafer *i.e.*, the sample is aligned and exposed by a mask aligner system. The short wavelength of ultraviolet source *i.e.*, 456 or 654 nm is used for the exposure, and then the sample is developed by an appropriate developer followed by cleaning the same in DI water.

The sensor materials, *i.e.*, spin-valve structure Ta(5)/NiFe(10)/Cu(1.5)/NiFe(2)/IrMn(10)/Ta(5) (nm), is deposited on the stenciled photoresist layer by using magnetron sputtering system. The base pressure of the system is less than 10^{-7} Torr and the Ar working pressure is 3 mTorr. During the deposition, a uniform magnetic field of 200 Oe was applied in the thin film plane to induce magnetic anisotropy of the ferromagnetic pinned layer and to define the unidirectional field of the thin films. After the thin film deposition, the sample was lifted off in acetone and methanol solutions in order to remove the photoresist as well as the sensor material on this photoresist, so that the sensor material exists on the stenciled junctions only.

After fabricating sensor junctions, the electrodes made by Au are connected with sensor junction to establish the external circuitry and to measure the sensors' response. Further, the sensor junctions and the electrodes are passivated with a SiO$_2$ or a Si$_3$N$_4$ layer coated on top of the sensor junctions and electrodes to protect them from the corrosion and fluid environment during the experiments. Finally, the sensor is activated by a very thin Au layer for biomolecule immobilization. All these steps are carried out at the same way for all the sensors as the steps for the sensor junction fabrication.
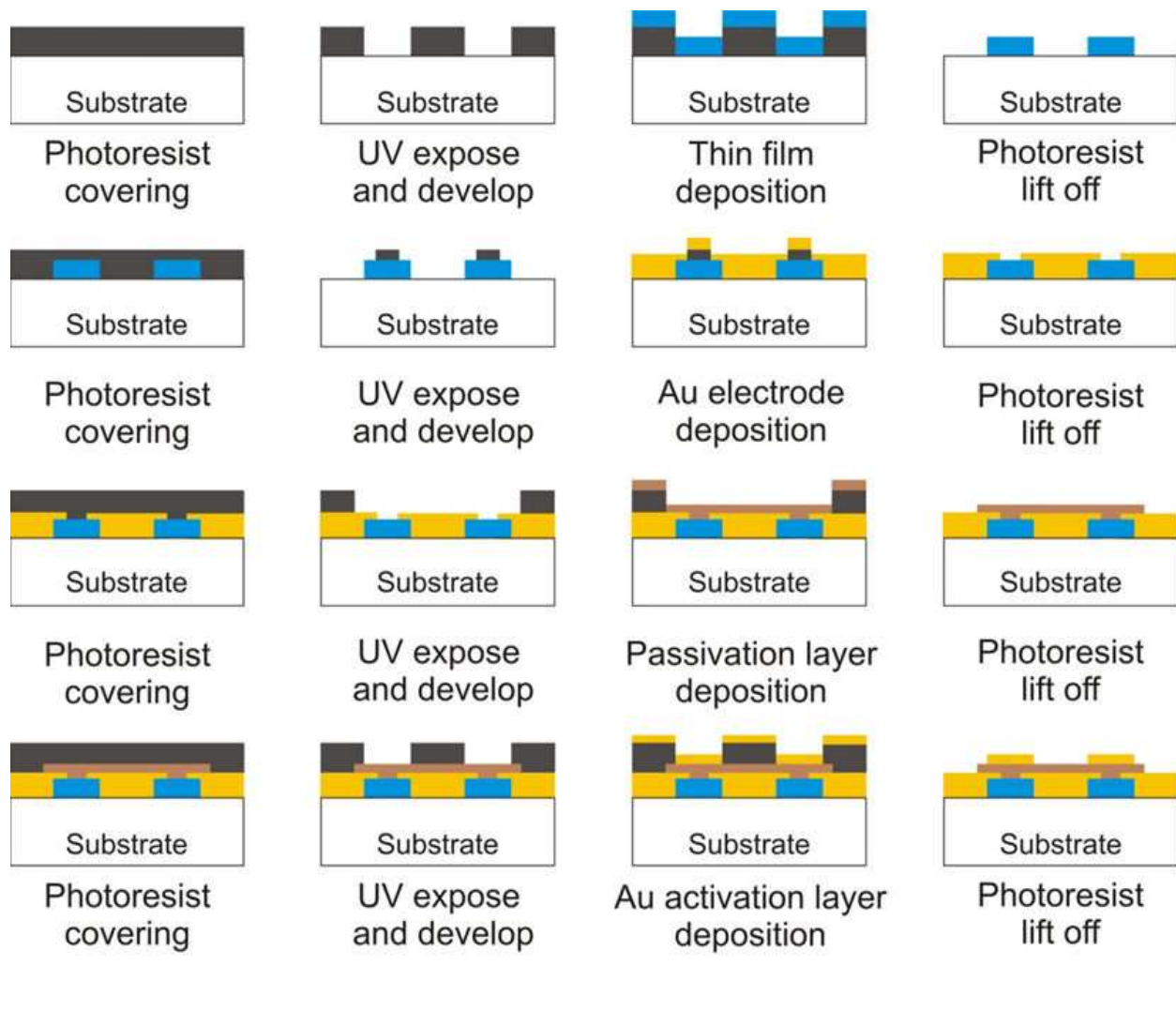
Figure 2. The pattern processes for fabricating the sensor junction, electrodes, passivation and Au activation layers of a planar Hall sensor, this sensor is ready for bio-manipulation.

3.2. Sensor characterization

The quality of the spin-valve structure, Ta(3)/NiFe(10)/Cu(1.5)/NiFe(2)/IrMn(10)/Ta(3) (nm), as observed by a cross sectional transmission electron microscope (TEM) image and also by an energy dispersive X-ray (EDX) spectrum along its thickness, are shown in Fig. 3. The TEM-specimen was prepared by polishing the Si/SiO_2 substrate mechanically to a thickness of about 100 μm. After that, the dimpling and hollowing steps were performed at the optimum conditions to ensure that the sample is undamaged by using a GATAN-691 precision ion polishing system (PIPS), *i.e.*, using the Ar-ion beam with an energy of 4.3 keV and under an angle of 6°.

It is evident from Fig. 3(a) that the existence of a multilayer structure is clearly revealed as pointed out by an arrow for each layer. The both seed and top layers of Ta have amorphous

behavior and the thickness is about 3 nm. However, there is a difference in the color of the two layers; this can be assumed that the Ta top layer is slightly oxidized [20]. The IrMn layer is well defined, and its thickness is about 10 nm as the nominal thickness when the layer is deposited. In the NiFe/Cu/NiFe region, it is clearly seen that the diffusion of Cu takes place into the adjacent NiFe layers. This kind of diffusion is known to influence the anisotropy significantly [21]. There is also an existence of a rumpling or even a rupture of the layers in some parts. This can be explained when considering the roughness of the NiFe layers; the roughness of NiFe layer is normally about 1.5 – 2 nm [22].
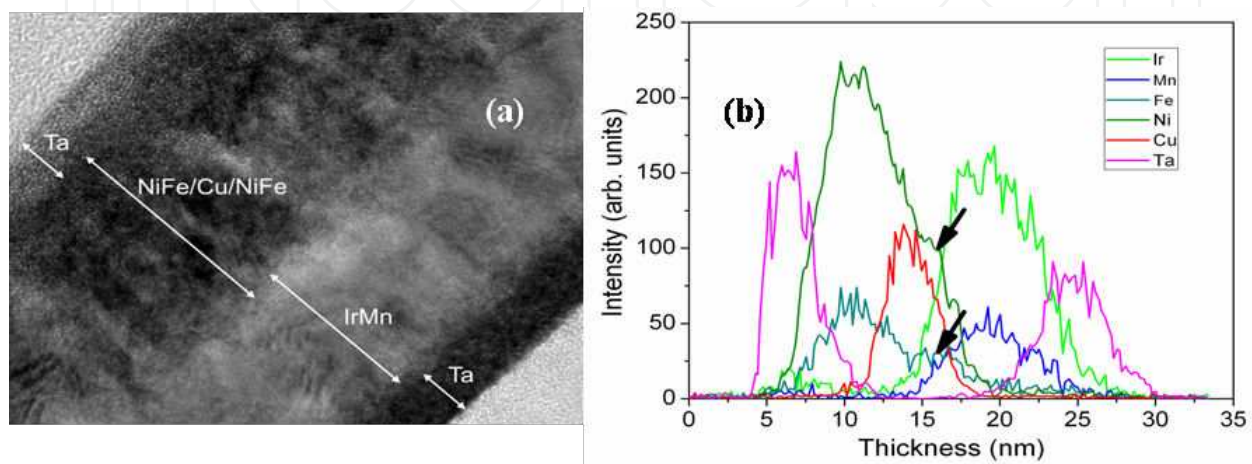
Figure 3. A cross sectional TEM image (a) and an EDX spectra (b) of a spin-valve structure Ta(3)/NiFe(10)/Cu(1.5)/ NiFe(2)/IrMn(10)/Ta(3) (nm).

The result of the cross sectional TEM image is supported by the EDX patterns of the same sample shown in Fig 3(b). It can be seen that the peak of Cu is mixing inside the Ni and Fe peaks indicating the diffusion of Cu in NiFe layers. The overlap between the peaks of Ta and Ni (Fe), of Ta and Ir (Mn), and of Ir (Mn) and Ni (Fe) confirms the roughness at the surface of the NiFe and IrMn layers. Moreover, the shadow in Ni and Fe peaks (black arrows in Fig. 3(b)) indicates the separation of the NiFe pinned and NiFe free layers.

The magnetic property of the fabricated spin-valve structure used for sensor material is characterized by a vibrating sample magnetometer (VSM) of the make Lakeshore 7407 series with a sensitivity of 10^{-6} emu. The external magnetic field is swept in the film plane.

In order to achieve the magnetic anisotropy of the free layer in the fabricated spin-valve structure, we measured the magnetization as a function of external magnetic field in the range of ± 80 Oe in both the easy and hard axis, which is presented in Fig. 4. The shift along the external magnetic field axis of the magnetization profile ($M(H)$) in the easy axis indicates an effective uniaxial anisotropy field of the spin-valve structure (H_{Keff}) by incorporating the free layer shape anisotropy field ($H_{demag.}$) and its uniaxial anisotropy field (H_K) analyzed from the shift of the $M(H)$ profile in the hard axis ($H_{Keff} = H_K + H_{demag.}$) [23]. This indicates that the free NiFe layer (active layer) has very good anisotropy characteristic for further study of the PHE sensor. In addition, the inset in Fig. 4 exhibits a two-step hysteresis loop;

one is from the interlayer coupling and the other is from the exchange bias coupling. The magnetization of the first hysteresis loop (contributing from 10 nm NiFe free layer) is five times larger than the second one (contributing from 2 nm NiFe pinned layer). The interlayer coupling between the ferromagnetic (F)-free and F-pinned layers separated by a non-magnetic layer (Cu) is determined from the first step of the hysteresis loop. Whereas, the exchange bias field due to the interface between the F-pinned and antiferromagnetic (AF) layers is determined from the second step of the hysteresis loop. The obtained interlayer and interfacial coupling fields are 11 Oe and 550 Oe, respectively. This result elucidates that the NiFe pinned and NiFe free layers are separated by a Cu layer.
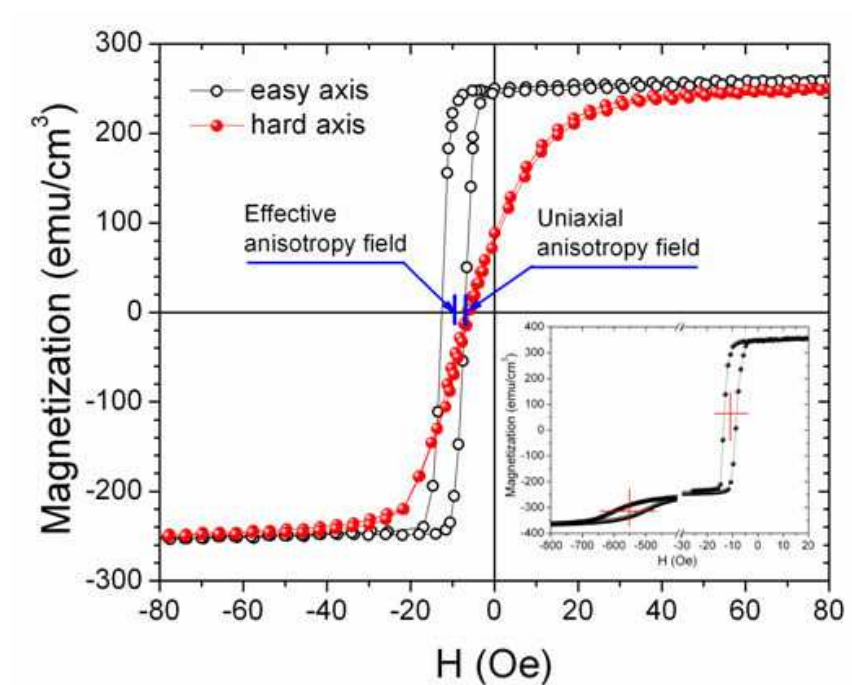
Figure 4. Hysteresis loops of the spin-valve thin film, Ta(3)/NiFe(10)/Cu(1.5)/NiFe(2)/IrMn(10)/Ta(3) (nm), characterized in the easy and hard axis in the field interval from + 80 to -80 Oe. The inset shows the hysteresis loop characterized in the easy direction in the field range of -800 to 20 Oe.

3.2.1. Microarray of the magnetic sensors

Fig. 5 shows a complete micro-array of planar Hall resistance (PHR) sensors. In the figure, it was shown that the unidirectional field, H_{ex}, and/or the uniaxial field of the thin film were aligned parallel to the terminals a–b, and a sensing current of 1mA was applied through these terminals. The output voltages were measured from the terminals c and d at room temperature under a specific range of external magnetic field applied normal to the direction of the current.
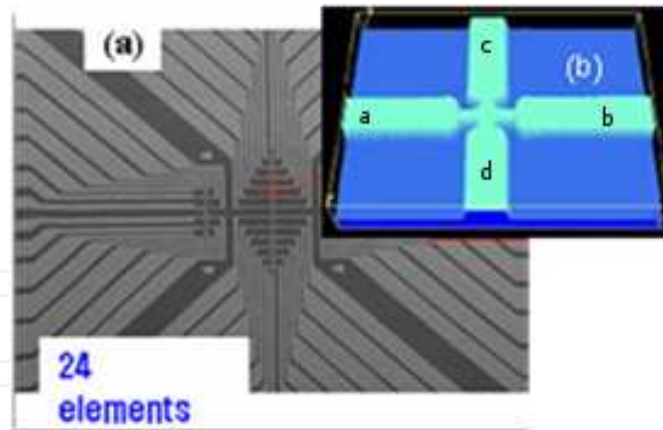
Figure 5. Complete micro-array of a 24 element PHR sensor(a), which can even detect a single micro-paramagnetic Dynabead M®-280. Inset of the figure (b) shows a single micro sized cross-junction.

4. Evolution of novel PHR sensors

Among all the developed magnetoresistive sensors for bioapplications, we mainly focus on the development of PHE sensor because it has prominent advantages compared with others such as signal-to-noise ratio, linearity signal *etc*. Various structures will be used for planar Hall sensor *i.e.*, bilayer, trilayer and spin-valve. Therefore, a short introduction of these multilayer structures will be given in this section. Also, the theoretical approach of planar Hall effect in different sensor geometries, such as cross-junction, tilted cross-junction and ring junction, will be discussed. Finally, the description leads to evolution of hybrid AMR-PHR sensor with optimized sensor characteristics for effective use in bioapplications.

4.1. AMR sensor

The magteoresistive anisotropy in ferromagnetic material depends on the direction of magnetization. The electric field due to the magnetoresistivity is expressed as follows [24];

$$\vec{E} = \rho_{\perp}\vec{j} + (\rho_{ll} - \rho_{\perp})\vec{m}(\vec{j} \cdot \vec{m}) \tag{3}$$

where $\vec{m}$ is magnetization vector in single domain, and $\vec{j}$ is current density direction. The ρ and $\rho_{//}$ are the resistivity when the magnetization vector and current density direction are perpendicular and parallel, respectively. The $\Delta\rho = \rho_{//} - \rho$ is defined by the anisotropic resistivity, which is the intrinsic resistivity by the spin-orbit scattering in ferromagnetic materials. In Eq. (3), the electric field can be measured in the current direction as well as perpendicular to current direction due to the anisotropic resistivity, which are called, as mentioned, as the AMR and PHR, respectively.

The AMR properties have been discovered at ferromagnetic material by William Thomson in 1857 [25]. In the AMR response, varying differences between the direction of the magnetizing vector in the ferromagnetic film and the direction of the sensing current passing through the film lead to varying the resistance in the direction of the current. The maximum resistance occurs when the magnetization vector in the film and the current direction are parallel to one another, while the minimum resistance occurs when they are perpendicular to one another. The resistance change by AMR effect in the patterned film with thickness t, width w and length l can be expressed from Eq. (3).

$$V_{AMR} = I(R_\perp + \Delta R \cos^2 \theta)$$ (4)

where $\Delta R = (\rho_{ll} - \rho_\perp)l / \omega t$ is the anisotropic magnetoresitivity and the θ is the angle between the magnetization vector and current, I. In AMR effect, the MR ratio is expressed as $\Delta R / R_\perp \times 100$. The AMR effect has an offset resistance of $R_\perp$. This offset resistance must be reduced to improve the performance by using a compensating voltage or a Wheatstone bridge circuit [26].

4.2. Planar Hall resistance sensor

The planar Hall resistance (PHR) in ferromagnetic thin films was considered when the resistivity depends on the angle between the direction of the current density j and the magnetization m. For magnetization reversal of the single domain when m makes an angle θ with j, the electric field is described as follows;

$$E_{PHR} = j(\rho_{//} - \rho_\perp) \sin \theta \cos \theta$$ (5)

The PHR effect also varies when there is a difference between the direction of the magnetizing vector in the ferromagnetic film and the direction of the sensing current passing through the film; however, it leads to varying the resistance in the perpendicular direction of the current only. The longitudinal component of PHR voltage is related to E_{PHR} in Eq. (3) and can be revealed when anisotropy of resistivity exists. On the other hand, in this sensor, the measured PHR voltage was described as follows:

$$V_{PHR} = \frac{I(\rho_{ll} - \rho_\perp)}{t} \sin \theta \cos \theta$$ (6)

where t is the thickness of ferromagnetic film. The PHR in Eq. (6) varies with the angle θ. The PHR does not impose the offset resistance. Therefore, it has the advantage of obtaining a large PHR ratio and a linear response characteristic when the angle θ having a small value. The PHR effect depends on the intrinsic magneto-resistivity, $\Delta \rho = \rho_{ll} - \rho_\perp$ and the sample

thickness, t. This means that the PHR signal does not depend on the sensor size (width ω and length l). Therefore, the PHR sensor can be used as the micro- or nano sized sensor for the micro- or nano- bead detection maintaining the large output signal voltage.

In order to analyze the PHR signal with magnetic field, we must know the angle θ between the magnetization vector and current direction, which depends on the magnetic field. Fig. 6 shows the general coordinates used to describe the rotational magnetization process under the applied magnetic field in ferromagnetic/antiferromagnetic (F/AF) coupled samples. H_{ex} is the exchange coupling field due to the antiferromagnetic layer, and it shows a biasing field effect. K_u is the effective in-plane anisotropy constant with an angle γ from H_{ex}.
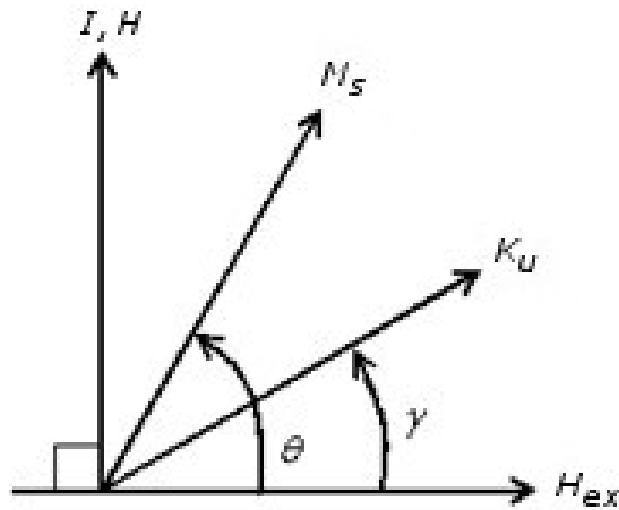

Figure 6. The coordinates for domain rotation process. Here, γ and θ are the angles of the anisotropy constant, and magnetization from the exchange-coupling field, H_{ex}, respectively, and I is the measuring current.

The applied magnetic field H is directed perpendicular to H_{ex}, and force the magnetization to rotate by an angle θ towards H. We introduce the modified Stoner-Wolfforth model with magnetic energy density, E_T for the F layer in the F/AF sample, which can be written in the following simple form [12, 27]

$$E_T = K_u \sin^2(\theta - \gamma) - HM_s \sin\theta - H_{ex}M_s \cos\theta \qquad (7)$$

where M_s is the saturation magnetization. The angle θ determines the orientation of the magnetization in an equilibrium state with minimum total energy, whose values are calculated under the conditions of $\partial E_T/\partial\theta = 0$.
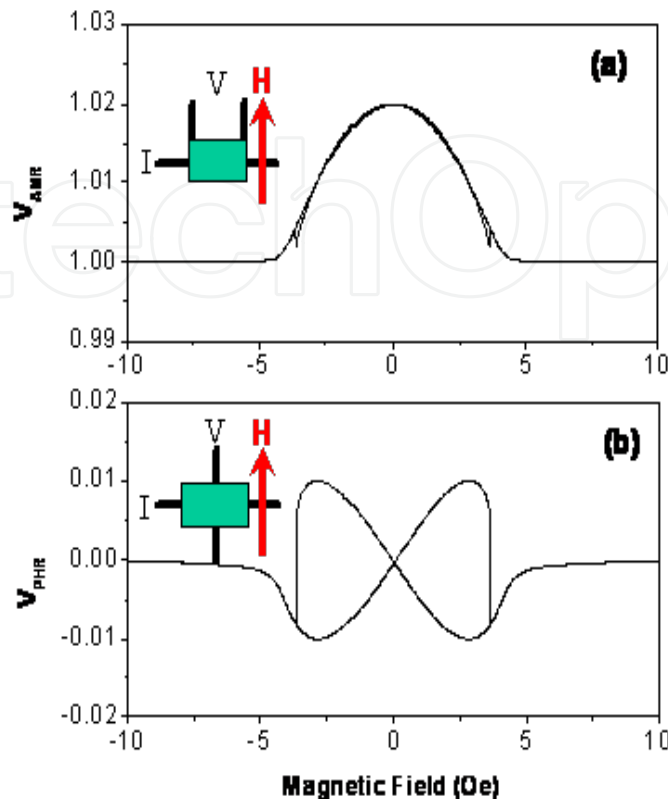
Figure 7. (a) Calculated V_{AMR} and (b) V_{PHR} with applied magnetic field in single ferromagnetic film

Fig. 7 shows the calculated V_{AMR} and V_{PHR} in ferromagnetic single layer without exchange bias field, H_{ex}. The measuring configuration of AMR and PHR voltage is shown in the inset of the figures. The current was applied parallel to the easy axis and the magnetic field was applied parallel to the hard axis of the magnetic thin film. The AMR voltage was measured in the direction of the sensing current passing through the film, while the PHR voltage was measured in the perpendicular direction of the sensing current. In the case of AMR effect, the signal shows the symmetric behavior in the functions of applied magnetic field with off-set voltage of $R_\perp$. The PHR signal shows the linear behavior in the functions of applied magnetic field with zero offset voltage.

Therefore, the PHR sensor justifies that it can be used as the micro- or nano- sized magnetic field sensor for the detection of the micro- or nano- bead. The PHR signal in ferromagnetic single layer shows large hysteresis behavior. The hysteresis effect is due to the switching of the magnetization in ferromagnetic layer. In order to remove the hysteresis of PHR, the exchange biased F/AF bilayers are considered.

4.3. PHR effect in exchange biased F/AF multilayer structures

The single ferromagnetic layer with high AMR ratio such as NiFe, CoFe and NiCo alloys has the uniaxial anisotropy. The easy axes for stable magnetization direction are 0 and 180 degrees. If one cycle of magnetic field is applied in the perpendicular direction to the easy axis in ferromagnetic films, the magnetization direction changes from 0 to 90 degrees as the magnetic field increases, and 90 to 180 degrees as the magnetic field decreases. And then the direction of the magnetization changes from 180 to 270 and then to 360 degrees as the reversed magnetic field increases and decreases. In that case, the AMR and PHR, which are dependent on the angle between the current and magnetization directions, can show the large hysteresis loop. On the other hand, the exchange biased F/AF bilayers induce the unidirectional anisotropy, which rotates the magnetization direction from 0 to 90 and 90 to 0 degrees as the magnetic field increases and decreases, respectively. It means that the AMR and PHR signal in exchange biased F/AF bilayers show the reversal behavior and the hysteresis can be disappeared.
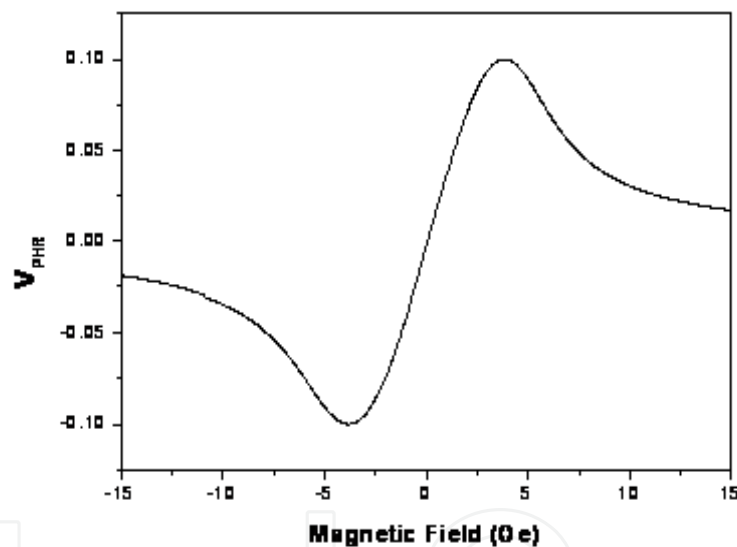

Figure 8. V_{PHR} signal with applied magnetic field in exchange biased F/AF bilayers

Fig. 8 shows the calculated PHR signal for the exchange biased F/AF bilayers. By comparing the PHR signal of the exchange biased F/AF bilayers in Fig. 8 with that of the single ferromagnetic layer in Fig. 7(b), we can clearly confirm that no hysteresis behavior of PHR signal takes place in exchange biased F/AF bilayers. The exchange bias field, H_{ex} plays the role of the reversible rotation of the magnetization as the magnetic field changes, which is due to the unidirectional anisotropy compared with the uniaxial anisotropy in single ferromagnetic layer. Also the reversible rotation of the magnetization in exchange biased F/AF bilayers can reduce the Barkhausen noise, which is usually dominated in the irreversible domain motion. Therefore, the signal to noise ratio (S/N ratio) of PHR sensor can be increased by using the

exchange biased F/AF bilayers. Further, the PHR effect in exchange biased bilayers shows good linearity and thus it has the advantage for magnetic field sensor application. In the case of GMR or TMR materials, though they have high MR ratios, however, theirs' linearity is not good compared with the PHR signal. Therefore, PHR effect in the exchange biased F/AF bilayers has advantages in use as a bio-sensor for micro or nano bead detection.

4.3.1. Bilayers

There exists an interfacial coupling in F/AF bilayers. The hysteresis loop of the F layer, instead of being centered at zero magnetic field, is now displaced from $H = 0$ by an amount noted as the exchange field H_{ex}, as if the F layer is under a biased magnetic field. Hence, this phenomenon is also known as exchange bias [28]. In such a structure the anisotropy may behave as unidirectional anisotropy. Technologically, exchange bias is of crucial importance in the field-sensing devices. An example $M(H)$ loop of Ta(3)/NiFe(10)/IrMn(10)/Ta(3) (nm), which is usually the structure being used for fabricating a sensor, is used for this study. The center of the hysteresis loop of this bilayer, as shown in Fig. 9, is shifted from zero applied magnetic field by an amount H_{ex}, the exchange bias field.
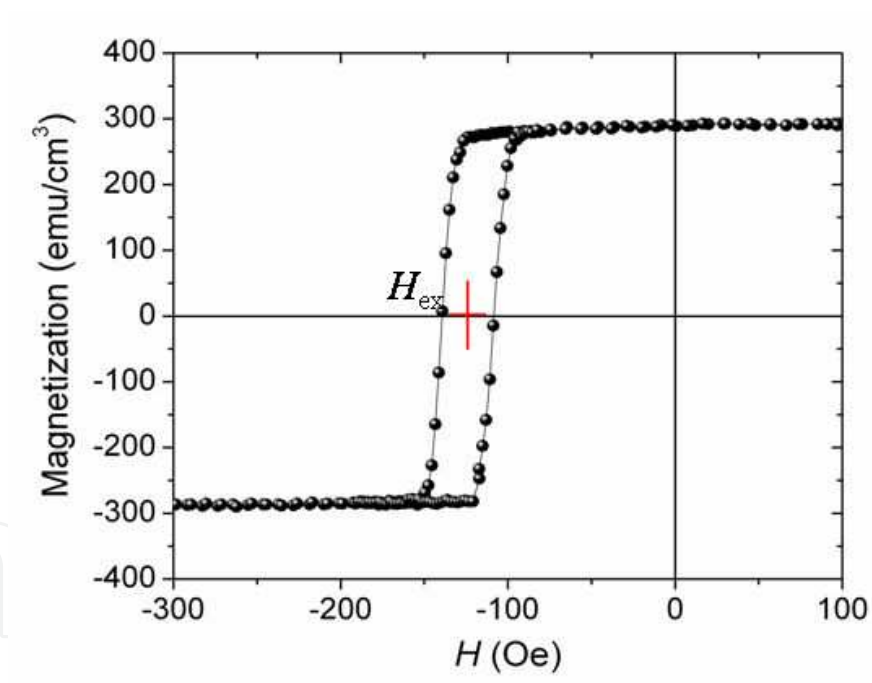
Figure 9. The shifted hysteresis loop in an exchange biased bilayer thin film

In a bilayer structure, the exchange coupling between the F and AF layers can easily induce the unidirectional magnetic anisotropy of the F layer. In addition, the F layer is improved to be constrained to the magnetization in coherent rotation towards the applied fields, so the sensor can prevent Barkhausen noise associated with the magnetization reversal, and improves the thermal stability [29]. Because of these advantages, a bilayer structure is a good candidate for developing sensor materials.

Bilayer has been used as PHE sensor materials by M.F. Hansen *et al*, C.G. Kim *et al*, and F.N.V. Dau *et al*. It is revealed from the literature that the sensitivity of a PHE sensor is increased with the thickness of ferromagnetic layer up to 20 nm [27].

4.3.2. Spin-valves

The spin-valve structure, as shown in Fig. 10(a), which was known as a simple embodiment of the GMR effect, typically consists of two F layers separated by a nonmagnetic conductor whose thickness is smaller than the mean-free path of electrons. The magnetic layers are uncoupled or weakly coupled in contrast to the generally strong AF state interaction in Fe-Cr-like multilayer; thus the magnetization of F layer with uniaxial anisotropy can be rotated freely by a small applied magnetic field in the film plane, while the magnetization of other magnetic layer had unidirectional anisotropy and was pinned by exchange bias coupling from AF layer. If the relative angle between the magnetization of the two layers changes, a giant magnetoresistance change occurs.

In an illustrative demonstration of the operation of the spin-valve, the applied magnetic field is directed parallel to the exchange biased field and cycled in magnitude. The $M(H)$ loop and the corresponding magnetoresistance curves are shown schematically in Fig. 10(b) and (c), respectively.
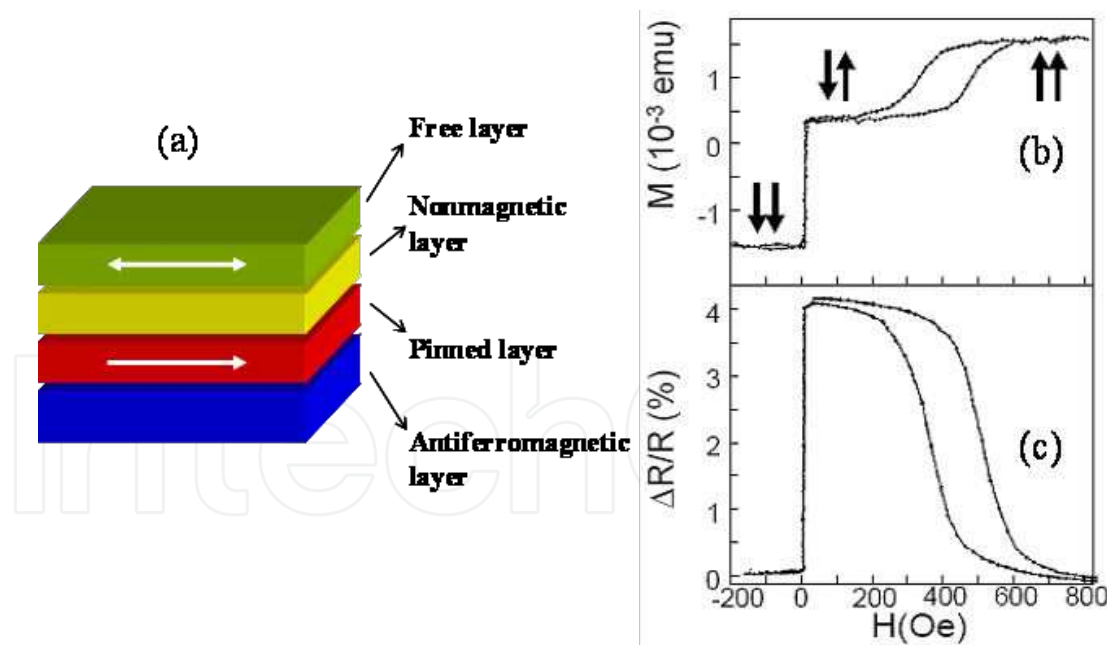
Figure 10. (a) Schematic of a typical spin-valve structure, (b) Hysteresis loop, and (c) magnetoresistance of a spin-valve sample of composition, Ta(5)/NiFe(6)/Cu(2.2)/NiFe(4)/FeMn(7)/Ta(5) (nm), at room temperature [27, 30].

The sharp magnetization reversal near zero magnetic field is due to the switching of the free magnetic layer in the presence of its weak coupling to pinned magnetic layer. The more rounded magnetization reversal at higher magnetic field is due to the switching of the pin-

ned magnetic layer, which overcomes its exchange biased coupling to an AF layer for these fields. Therefore, it was emphasized that a spin-valve here makes use of two different exchange couplings; exchange biased coupling from pinned layer to AF layer and interlayer exchange coupling between two magnetic layers, which in origin, was tentatively assigned to a Ruderman–Kittel–Kasuya–Yosida (RKKY) interaction. The relative orientations of two magnetic layers were indicated by the pairs of arrows in each region of the $M(H)$ curve where the resistance is larger for antiparallel alignment of the two magnetic layers.

In order to optimize the spin-valve structure for high sensitivity PHE sensor, Kim's group has investigated systematically the effect of the thickness of F-pined and F-free layers (t_f and t_p) in the spin-valve structure Ta(5)/NiFe(t_f)/Cu(1.2)/NiFe(t_p)/IrMn(10)/Ta(5) (nm) with t_f = 4, 8, 10, 12, 16, 20 nm, and t_p = 1, 2, 6, 9, 12 nm. The results show that the sensitivity is increased linearly with t_f and is decreased exponentially with t_p in the investigated range. As the result, the optimized spin-valve structure for highest sensitivity is Ta(5)/NiFe(20)/Cu(1.2)/NiFe(1)/IrMn(10)/Ta(5) (nm). The details explanation could be found in Ref 13.
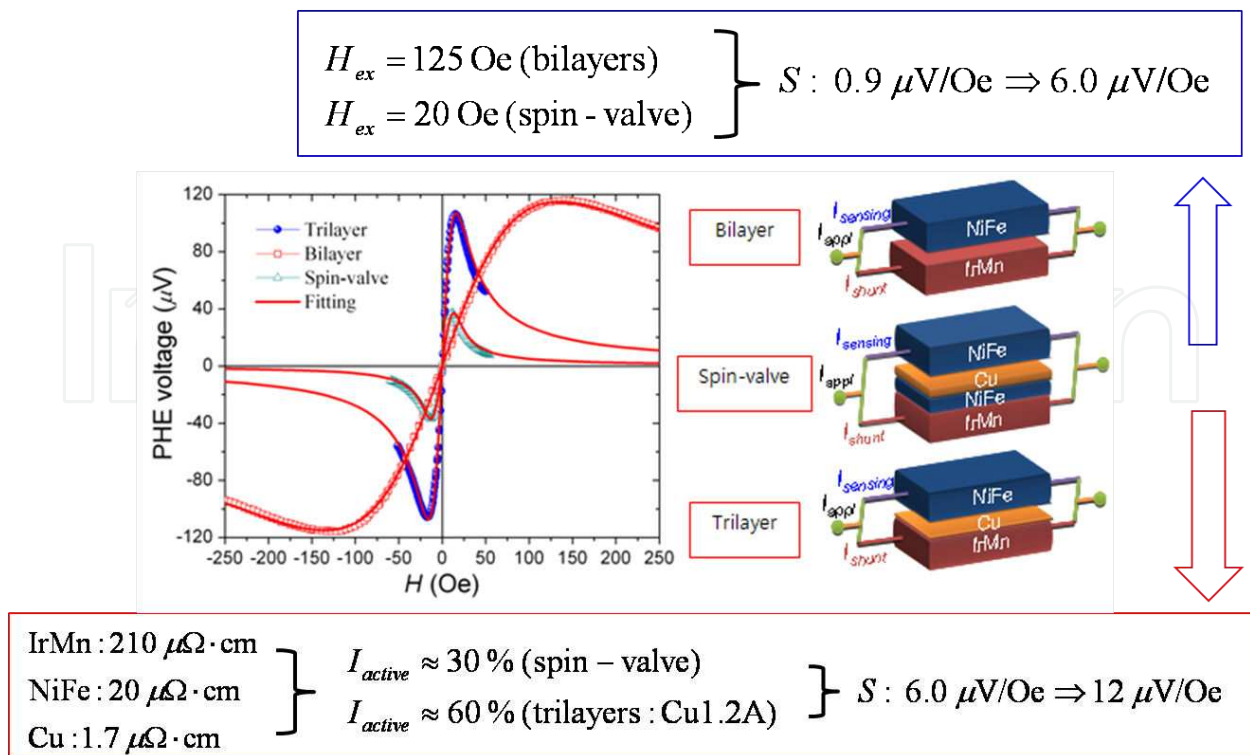
4.3.3. Trilayers

The origin of interlayer coupling in F/spacer/AF trilayer structure is totally different from interlayer coupling induced in F/spacer/F multilayer thin films. The observation of F/AF exchange coupling across a nonmagnetic layer by Gökemeijer *et al.*, [31] demonstrates that the exchange bias is a long-range interaction extending to several tens of Å. This coupling is not oscillatory but decays exponentially as $J \sim \exp(-t/L)$. The range of F/AF exchange coupling is specific to the spacer material, and thus most likely electronic in nature.

In our experiment, we choose Cu as spacer layer in the trilayer structure, Ta(3)/NiFe(10)/Cu(0.12)/IrMn(10) (nm), because it gives a small exchange coupling with a thin Cu layer. In the sensor application, it can reduce the shunt current resulting in enhanced sensitivity. The exchange coupling of the trilayer structure, determined by the shift of the hysteresis loop in the magnetic field direction and is measured in the order of few tens of Oe, is one order smaller compared with the exchange coupling in a typical bilayer structure (in order of hundred Oe) as shown in Fig. 9. A comparison of the PHE voltages generated by the bilayer, spin-valve and trilayer structures and their corresponding sensitivities are shown in Fig. 11. Thus, it can be easily seen from the figure that the trilayer structure can improve the field sensitivity of a sensor better than those of the bilayer and spin-valve structures [32].

4.4. Sensor geometry

The performance of the sensor depends largely on its physical geometry. There were several geometries reported in the literature in the design of planar Hall sensor. Among these geometries, the cross-junction and circular geometries need special mention as they result better performance of the sensor. Thus, it is intended to present the results of the sensor for better understanding of the sensor performance when the geometries are explored in the form of cross-junction, tilted cross-junction and circular ring junction.

$$H_{ex} = 125 \, \text{Oe (bilayers)}$$
$$H_{ex} = 20 \, \text{Oe (spin - valve)}$$
$$S : 0.9 \, \mu\text{V/Oe} \Rightarrow 6.0 \, \mu\text{V/Oe}$$

$$IrMn : 210 \, \mu\Omega \cdot cm$$
$$NiFe : 20 \, \mu\Omega \cdot cm$$
$$Cu : 1.7 \, \mu\Omega \cdot cm$$
$$I_{active} \approx 30 \, \% \, (\text{spin} - \text{valve})$$
$$I_{active} \approx 60 \, \% \, (\text{trilayers} : Cu1.2A)$$
$$S : 6.0 \, \mu\text{V/Oe} \Rightarrow 12 \, \mu\text{V/Oe}$$

Figure 11. Comparison of the PHE performance between the bilayer, spin-valve and trilayer structures.

4.4.1. Cross-junction

In this part, we discuss the effect of the sensor size on the output voltage of a cross-junction PHE sensor.
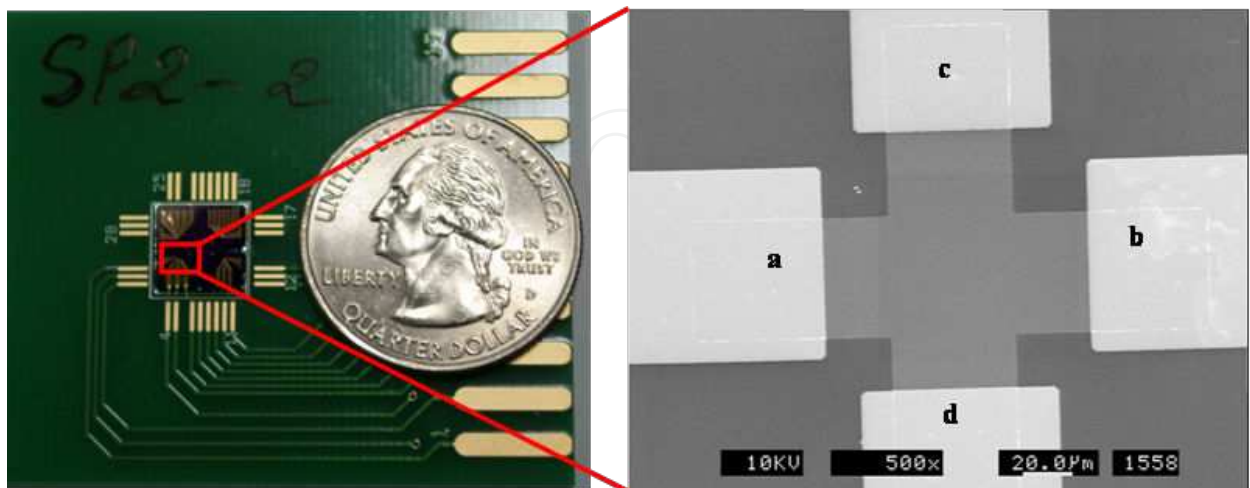
Figure 12. (left) Illustration of a fabricated PHR sensor, (right) top view micrograph of a single 50 μm × 50 μm PHE sensor junction

Fig. 12 (left) shows the illustration of a fabricated PHR sensor and the Fig.12 (right) shows the SEM image of the passivated single sensor cross-junction of the size 50 μm × 50 μm. The terminals *a-b* represents the current line and *c-d* represents the voltage line. The unidirectional anisotropy field, H_{ex}, and the uniaxial anisotropy field of the thin film are aligned parallel to the long terminals *a-b*. Planar Hall effect (PHE) profiles were measured by the electrodes bar *c-d* with a sensing current of 1 mA applied through the terminals *a-b* and under the external magnetic fields ranging from – 50 Oe to 50 Oe applied perpendicular to the direction of the current line and in sensor plane. The induced output voltages of cross-junctions were measured by means of a Keithley 2182A Nanovoltmeter with a sensitivity of 10 nV. All these sensor characterizations were carried out at room temperature.

For studying the size effect in planar Hall sensor, cross-junctions with various sizes of x × 50 μm^2 and 50 × x μm^2, (x = 30, 50, 100) using spin-valve structure Ta(3)/NiFe(10)/Cu(1.5)/NiFe(2)/IrMn(10)/Ta(3) (nm) were fabricated. For estimating the free layer magnetic anisotropy of the fabricated spin-valve structure, we measured the magnetization as a function of the external magnetic field in the range of ± 80 Oe in both the easy and hard axis (refer to Fig. 4). As mentioned, the shift along the field axis of the magnetization profile in the easy axis indicates that the free NiFe layer (active layer) has very good anisotropy characteristic for further studying the PHE voltage profiles of the sensor.

The PHE voltage profiles of the fabricated sensors with various junction sizes are given in Fig. 13. Analogous to the other PHE results, the PHE voltage in all the sensor junctions initially changes very fast and appears linear at low fields, reaches a maximal value at H ~ 11 Oe and finally decreases with further increase in the magnetic fields.
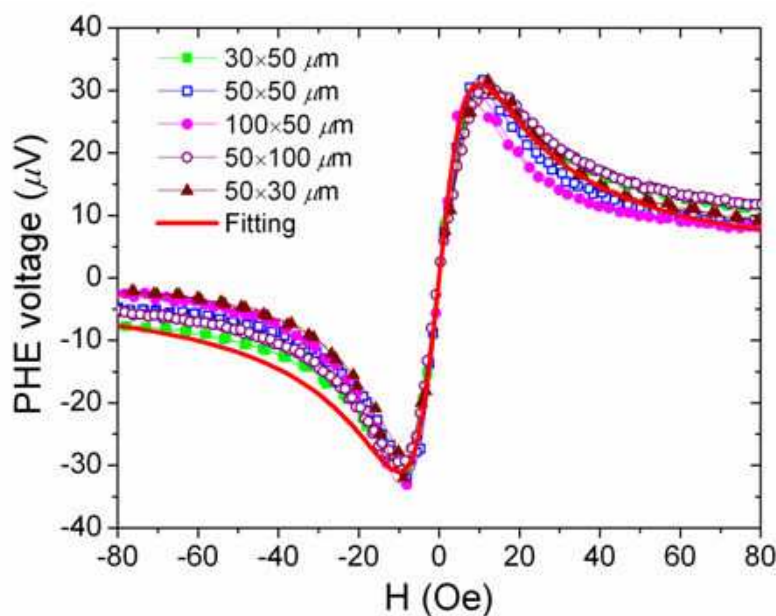
Figure 13. The PHE voltage profiles of the various size sensor junctions based on the spin-valve thin film Ta(3)/NiFe(10)/Cu(1.5)/NiFe(2)/IrMn(10)/Ta(3) (nm)

It is noteworthy that the maximum value of the PHE voltage profile is obtained at the field close to the effective uniaxial anisotropy field, H_{Keff}, of the free layer. This finding was studied systematically in a spin-valve structure and has been reported, previously [31-34]. Moreover, it is observed in the linear response region (at the field range from -11 Oe to 11 Oe) only despite having variation in the junction size, and the slope of the PHE voltage profile remains constant. That means there is no change in the field-sensitivity when the sensor junction is varied either in length or width.

The theoretical voltage profile of the fabricated PHE sensor was also calculated with a set of following parameters: $K_u = 2 \times 10^3$ erg/cm^3, $M_s = 800$ emu/cm^3 for the NiFe, $J = 1.8 \times 10^{-3}$ erg/cm^2 ($J = tM_sH_{int}$), $H_K = 2K_u/M_s$, $I = 1$ mA and $V_o = \dfrac{I(\rho_{//} - \rho_\perp)}{t} = 62$ μV and the calculated result is represented as solid line in Fig. 13. The excellent agreement between the theoretical and experimental results confirms the point that the field-sensitivity of the PHE sensor is independent of the size of the cross-junction.

This result is important for the bio-applications because the sensitive detection of low bimolecular concentration is proportional to the junction size.
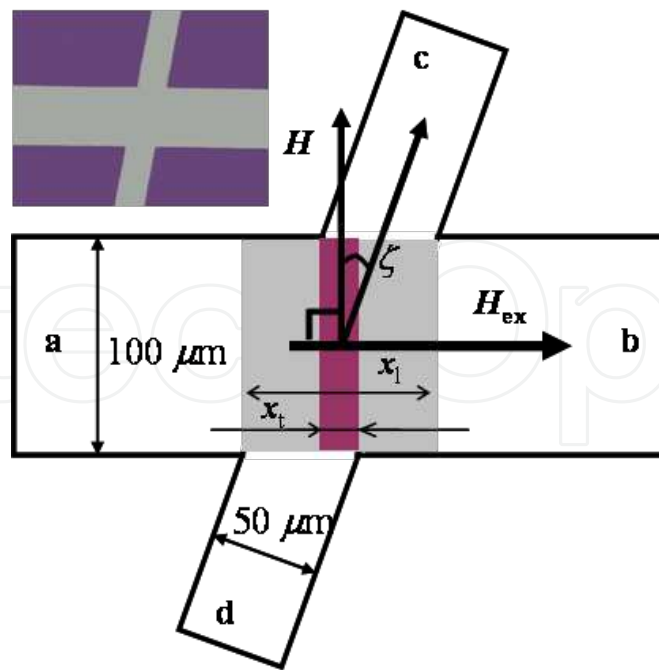
4.4.2. Tilted cross-junction

The idea behind the study of the tilted cross-junction is to combine some of the magnetoresistive effects, such as GMR, AMR and PHE and to explore how beneficial the sensor could be in its performance [35]. Therefore, the spin-valve structure which has GMR effect causing by spin scattering of electron between two F layers through a spacer layer, AMR and PHE effects causing by the spin-orbit coupling in the F layer are the best candidates for a sensor material.

To study the tilted cross-junction bars, 100 μm × 50 μm, with various tilt angles of $\zeta = 0°$, 4°, 8°, 10°, 30°, 45° using Ta(5)/NiFe(6)/Cu(3)/NiFe(3)/IrMn(15)/Ta(5) (nm) spin-valve structure are fabricated. The tilted cross-junction bar with a tilt angle ζ is shown in Fig. 14, in which the angle between the electrodes a–b and c–d is deliberately altered from 90° to 45°. The unidirectional field, H_{ex}, and the uniaxial field of the thin film were aligned parallel to the long terminals a-b, and sensing current of 1 mA was applied through these terminals. Output voltages were measured from the short terminals c and d at room temperature under the external magnetic fields ranging from - 45 Oe to 45 Oe applied normal to the direction of the current bar.

In general, the GMR and AMR effects could be obtained from the parallel direction to the current bar or longitudinal part while the PHE can be obtained from the transverse part of the sensor junction. Therefore, in a novel design of the sensor based on the tilted cross-junction the longitudinal and transverse contributions could be combined together in one sensor. In this tilted junction, we observed that there is an enhancement of PHE sensitivity and better linearlity of MR longitudinal component.

In Fig. 15 we demonstrated the output voltage profiles of the sensor junctions with different tilted angles. It clearly shows an increase in amplitude of the output voltage profile with increasing tilted angle ζ and the upward shift of the drift voltage. In particular, a significant en-

Figure 14. The geometry of a tilted cross-junction. The width of current and voltage bars are 100 μm and 50 μm, respectively. The inset shows the micrograph of the cross-junction with tilt angle ζ = 10°.

hancement of sensor sensitivity by about 30% is observed when the cross-junction is tilted with an angle of 45°, and in this case, the sensitivity about 9.5 μV/Oe is reached. It is also noteworthy to observe a gradual change in the shape of the output voltage profile from asymmetric to symmetric which implies a corresponding increase of longitudinal MR voltage due to the increment of tilted angle in the cross-junction, *i.e.*, for the first case when ζ = 0°, the voltage profile corresponds to the PHE only. In the other tilted cross-junctions ($\zeta \neq$ 0°), the output voltage profiles consist of the PHE, AMR and GMR components.

In order to understand the voltage contribution from each effect in a titled cross-junction quantitatively, we have performed systematic investigations on the role of the MR and PHE in the tilted cross-junction. In such case, it was noticed that the active PHE region and active MR region are from the transverse part and longitudinal part of the sensor, respectively. When the tilt angle of cross-junction increases, the length of the transverse part (x_t in Fig. 14) decreases and the length of longitudinal part (x_l in Fig. 14) increases accordingly.

It is observed that the PHE voltage is independent of the junction size irrespective of its change in the length or the width in previous part. Therefore, the PHE voltage component in the tilted cross-junction is always a constant. Then the transverse PHE component (corresponding to ζ = 0°) is decomposed from experimental data for different tilted cross-junctions. The decomposed results are illustrated in Fig. 16 for the sensor junction with ζ = 10°. Clearly, a strong contribution of the longitudinal MR component is evidenced. However, the PHE dominates good linearity and high sensitivity at low magnetic fields.
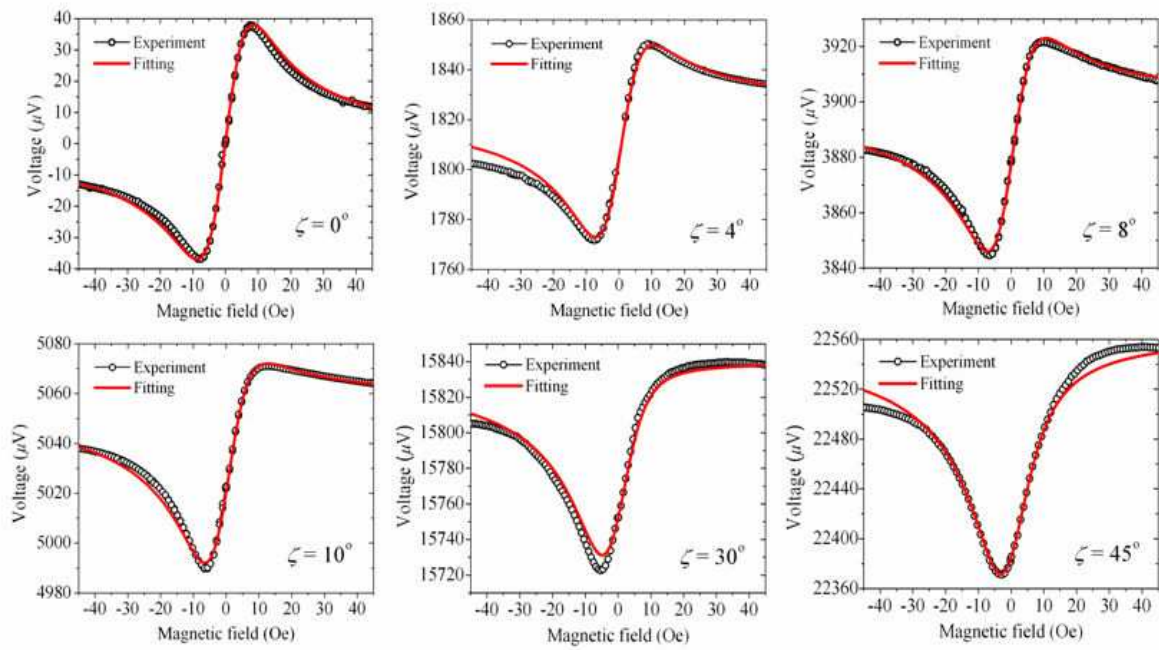
Figure 15. The experimental and theoretical voltage profiles of cross-junctions with different tilt angles of 0°, 4°, 8°, 10°, 30°, 45°.

Applying the above mentioned decomposition procedure for all investigated sensor junctions, one can derive the values of the drift (minimal) voltage (V_{MRmin}), the MR voltage (or the MR voltage change in external magnetic fields) ($\Delta V_{MR} = (V_{MRmax} - V_{MRmin})$) and the percentage of voltage change of the longitudinal MR voltage profile ($\Delta V_{MR}/V_{MRmin}$).

The results are listed in Table 2. Note that, V_{MRmin} and ΔV_{MR} increases as the tilted angle increases and thus the ΔV_{MR} enhances the total output voltage profiles.

ζ (°)	S (μV/Oe)	V_{MRmin} (μV)	ΔV_{MR}(μV)	$\Delta V_{MR}/V_{MRmin}$×100 (%)
0	7.4	-	-	-
4	7.5	1799	11.0	0.61
8	7.6	3877	24.0	0.62
10	7.7	5021	30.5	0.61
30	9.1	15752	94.5	0.60
45	9.5	22385	136.0	0.60

Table 2. The sensor sensitivity (S) and values of the minimal voltage (V_{MRmin}), MR voltage change in the applied fields (ΔV_{MR}), relative voltage change of the longitudinal MR voltage profile ($\Delta V_{MR}/V_{MRmin}$) of different tilted cross-junctions
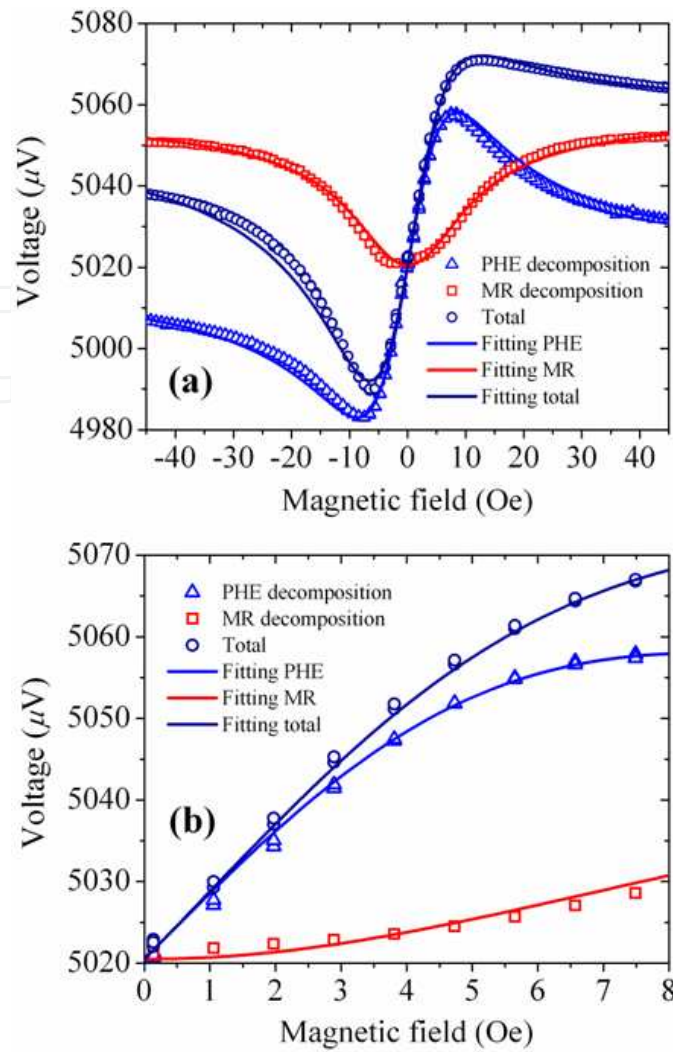
Figure 16. PHE and MR voltage components are decomposed from the experimental voltage profile of the sensor junction with the tilt angle $\zeta = 10°$ (a) at the field range of ±45 Oe and (b) at the field ranging from 0 to 8 Oe to illustrate the linearity of the sensor. In this figure, the origin of the PHE voltage component is adjusted to the minimum voltage of the MR components.

Generally, the longitudinal MR component was contributed from AMR and GMR effects [25,36]. The total output voltage induced from these effects satisfies the following equation [33]:

$$V_{MR} = I \times R_s \times \sin\zeta \times (1 + 0.5 \times GMR \times (1 - \cos(\theta - \theta_p)) + AMR \times \cos^2\theta) \qquad (8)$$

In this equation, θ_p is the angle between the magnetization direction of the F-pinned layer and the easy axis of F-free layer, and the drift voltage term ($I \times R_s \times \sin\zeta$) was modified from Ref. [33] in accordance with the investigated sensor junctions, because it depends on the length of the sensor junction. The increased length of the active region of the MR compo-

nents depends on the sinusoidal function of tilt angle ζ. From Eq. (8), if the sensor junction has no tilt angle, V_{MR} is zero, in which case the sensor has only the PHE contribution. When the junction starts to tilt, the MR components contribute to the total sensor output voltage. The drift voltage and then the MR voltage depend on sinusoidal function of the tilt angle ($\sim I \times R_s \times \sin\zeta$) [37].

The decomposed MR voltage profiles can be described with values of the sheet resistance R_s = 28.5 Ω, GMR = 1.8 % and AMR = 0.4 %. Other parameters are kept the same as for the PHE voltage profile calculations. The trend of the calculated results of representative sensor junction with $\zeta = 10°$ is presented by the red solid line in Fig. 16.

Finally, the total output voltage profiles of the tilted junctions are calculated by combining both the PHE and MR components represented in Eq. (8). The results are shown by solid lines in Fig. 16, where the calculated drift voltages are adjusted to the experimental drift voltages. It is clearly evident that a rather good consistence between the experimental and the calculated data is obtained. Thus, the tilted cross-junction exhibited not only a better sensitivity in comparison with individual PHR sensor but also a better linearity compared with individual MR sensor.

4.4.3. Ring junction

The idea to develop the sensor based on a ring is to combine both the PHE and AMR components in one ring junction [38]; thus, the output voltage of the sensor can be enhanced. In the following, the role of the output signal as well as the optimization results will be discussed.

Firstly, for studying the role of the signal in the ring junction, we design the ring with different configurations. These rings have the same diameter of 300 μm and the same width of 20 μm. The illustration schemes and the tested results corresponding to each configuration using exchange biased structure Ta(3)/NiFe(50)/IrMn(10)/Ta(3) (nm) are given in Fig. 17
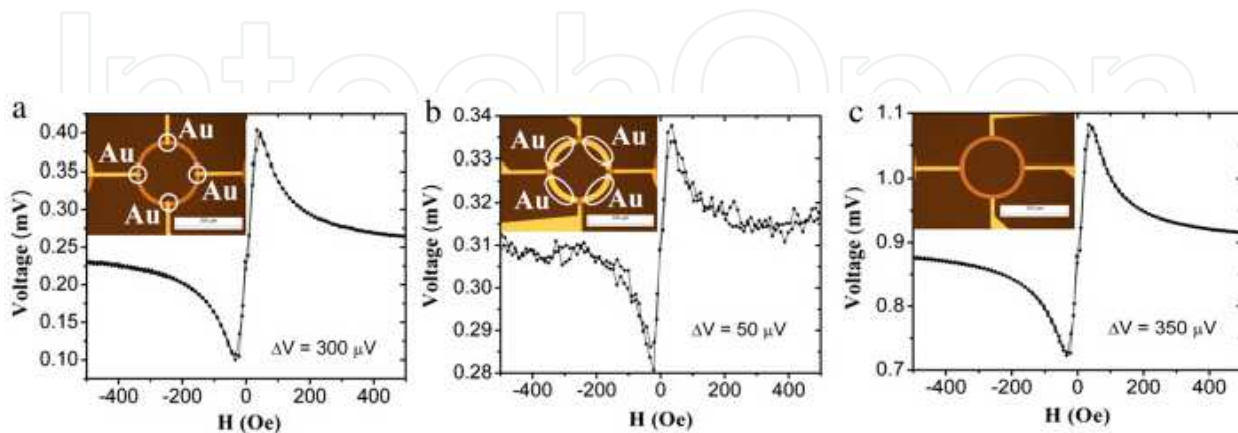
Figure 17. Designed rings with different Au electrode configurations and their corresponding output voltage profiles for the case of AMR arms (a), PHR elements (b) and a full ring (c) in the exchange biased structures shown in the inset.

It is evident from Fig. 17 that the signal change in the case of a full ring (350 μV) is close to the sum of the signals in the cases of a AMR arms (300 μV) and PHR elements (50 μV). Based on these obtained results we assume that, in the full ring junction, there exist two components AMR (Fig. 17(a)) and PHR (Fig. 17(b)).

4.5. Hybrid AMR and PHR ring sensor – Optimized performance

In order to optimize the performance of the sensor using a ring junction, efforts were made to design an hybrid AMR and PHR ring sensor. It is known that the maximum voltage of the AMR and PHR voltages in the ring can be calculated using:

$$
\begin{aligned}
V_{AMRo} &= \frac{r}{\omega}\frac{I\Delta\rho}{t} \\
V_{PHRo} &= \frac{I\Delta\rho}{t}
\end{aligned}
\tag{9}
$$

where r and ω are the radius and the width of the ring junction, I is the applied current, t is the thickness of the sensor material.

It is clear from the above that the PHR component is always constant while the AMR component increases linearity with the increase in r/ω ratio. It is noteworthy that when $r/\omega = 1$ the AMR voltage is equal to the PHR voltage, in which case the ring becomes the full disk. By fixing $I\Delta\rho/t = 1$, the output signal of the sensor is calculated, and the result is shown in Fig. 18.

The results in Fig. 18 ensure that the higher the r/ω ratio the larger the output voltage of the ring. To increase the r/ω ratio, basically, we can increase the radius, r, or reduce the width, ω, of the ring. However, for integrating with the other devices using present silicon technology, the ring size must be restrained to a certain limit. We assume that the ring size should be limited to about 300 μm, corresponding to the radius of $r = 150$ μm. The second problem that must be considered for optimizing the sensor performance is the width of the ring; the thinner the width, the higher the resistance, therefore, the higher output voltage can be achieved. But the width can not be made so thin, because the heat generated during the working time will burn the sensor junction. By considering these parameters, the optimized ring will have the radius of 150 μm and the width of 5 μm ($r/\omega = 30$).

The results of the sensitivity versus r/ω of the ring sensor using bilayer and trilayer structures (Ta(5)/Ru(1)/NiCo(10)/IrMn(10)Ru(1)/Ta(5) and Ta(3)/NiFe(10)/Cu(0.12)/IrMn(10)/Ta(3) (nm) are illustrated in Fig. 19. It is abundantly clear from the figure that the ring sensor using trilayer structure has higher sensitivity compared to that of bilayer structure. So the best performance of the ring is obtained using the trilayer structure, in which case the sensitivity is about 340 μV/Oe, and this is a much improved sensitivity compared to the sensitivity of an AMR or a PHR sensor (normally, the sensitivity of PHR sensor < 15 μV/Oe).
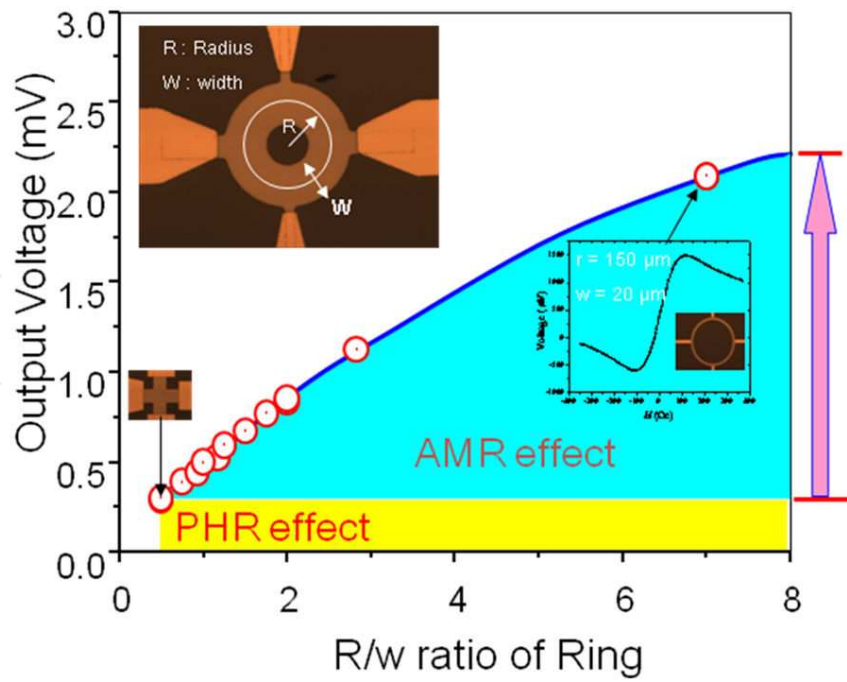
Figure 18. The calculation and experimental results of PHR and AMR output voltage components versus r/ω ratio of the ring. The insets show schematics of a ring junction with defined r and ω, and a representative PHE voltage profile of ring sensor for $r = 150\ \mu m$, $\omega = 20\ \mu m$.
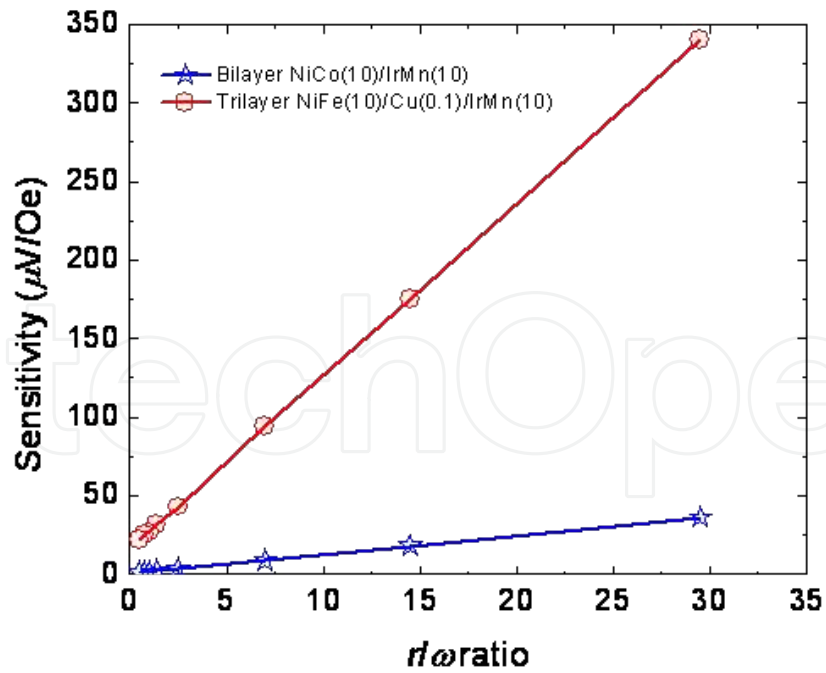
Figure 19. Experimental results of the sensitivity versus r/ω ratio of the rings using a Ta(5)/Ru(1)/NiCo(10)/IrMn(10)Ru(1)/Ta(5) (nm) bilayer thin film and trilayer thin film Ta(3)/NiFe(10)/Cu(0.12)/IrMn(10) /Ta(3) (nm).

It can be summarized from the above that the systematic investigations on the ring junctions revealed that there exist both PHR and AMR voltages contribute to the output voltage profile. The PHR voltage component is always kept constant when varying the size of the ring, while the AMR voltage component linearity increase due to the increasing the r/ω ratio of the ring. For practical and application aspects, the ring must be optimized both in terms of its size and performance. The optimized radius and the width of the junction are 150 μm and 5 μm, respectively. By using the trilayer structure, the best performance of the sensor is obtained. In such case, the highest sensitivity sensor is about 340 μV/Oe. This hybrid sensor is very much improved in the sensitivity compared to an AMR or a PHR sensor.

5. Biofunctionalized magnetic bead detection for state of the art lab-on-a-chip

Ever since the report of Baselt *et al.* on a magnetoresistive-based biochip with magnetic labels instead of fluorescent labels [3], the magnetic biochip has been extensively investigated as an advanced tool for sensitive detection of low bio-target concentration in body fluids for early diagnostics. Obviously, the focus in these investigations lies in development of a high sensitive magnetic field sensor that is optimized for magnetic label detection, and therefore different magnetoresistive sensing approaches, including the one that has just been described above i.e., hybrid AMR and PHR ring sensor, were adopted subsequently for this purpose. All these magnetic biosensors detect the stray field of magnetic particles that are bound to biological molecules. Since the biological environment is normally non-magnetic, the possibility of false signals being detected is negligible. In addition, the properties of magnetic particles are also stable over time and they may also be manipulated via magnetic forces, which can be produced by current lines that are fabricated into the chip itself. The advantages of magnetic labeling techniques have ultimately led the researchers to intensify their efforts in developing modern technologies for on-chip integration of micro- and nanoscale magnetics with molecular biology with a final goal of realizing highly sensitive, fast, reliable, cost-effective, portable and easy-to-use biomolecular sensor, the so called *magnetic lab-on-a-chip*.

5.1. Magnetic beads

Superparamagnetic nanoparticles coated with Streptavidin make ideal labels in bio-applications using magnetic sensors, because they can be readily magnetized to large magnetic moments. Most of our experiments were carried out with Dynabeads®M-280, which are composed of ultra small Fe_2O_3 nanopaticles embedded in a polymer matrix and the Streptavidin was conjugateed with the surface of the beads. The magnetization curve of the magnetic beads is shown in Fig. 20 [27, 39].
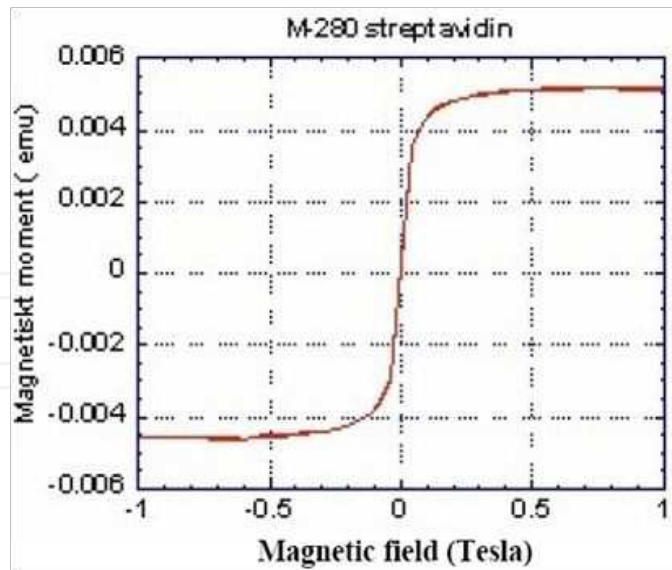
Figure 20. Magnetization curve of Dynabeads M-280 Streptavidin. This is supported by Dynal company.

When the magnetic bead appears on the sensor surface under an external magnetic field the magnetic field strength produced by a single bead can be estimated as [12, 14]

$$H = \frac{M R^3}{3r^3}(3(\hat{M} \cdot \hat{r})\hat{r} - \hat{M}) \tag{10}$$

where M, $\hat{M}$ are the magnitude and unit vector of magnetization. R is the bead radius, and r, $\hat{r}$ are the magnitude and unit vactor of the distance from the center of the bead to observation point as shown in Fig. 21.
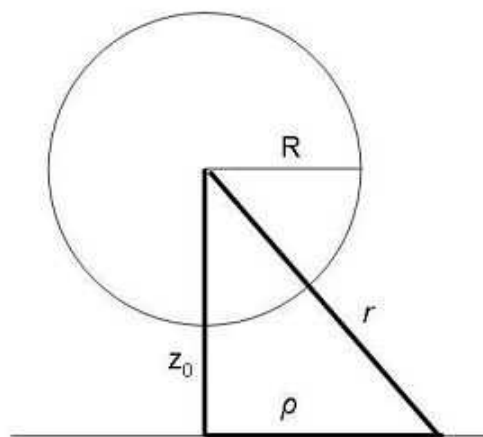
Figure 21. Schematic of a bead with the radius R placed above the sensor, r is the distance from the center of the bead to the observation point, z_o is the vertical distance from the center of the bead to the sensor, ρ is the distance in the sensor plane from the center of the bead to the observation point.

Assuming that the applied field is in x direction in a polar coordinate system then Eq. (10) can be rewritten as:

$$H_x = H \hat{x} = \frac{M R^3}{3r^3}(3\sin^2\theta\cos^2\varphi - 1) \tag{11}$$

with $\hat{x}\hat{r} = \sin\theta\cos\varphi$ and $\hat{x}M = 1$ when converting from polar coordinate system to spherical coordinate system.

Substituting $\sin\theta = \frac{\rho}{r}$ and $r = \sqrt{\rho^2 + z^2}$ into Eq. (11), H_x can be rewritten as

$$H_x = \frac{M R^3}{3}\frac{3\rho^2\cos^2\varphi - (\rho^2 + z_o^2)}{(\rho^2 + z_o^2)^5} \tag{12}$$

Following the Eq. (12), stray field of magnetic bead reaches maximum when $\rho = 0$, in this case $(H_x)_{max} = -\frac{M R^3}{z_o^3}$. This field reaches maximum at a right angle to the magnetization of the bead ($r \equiv z_o$ in Fig. 21) and decreases at other points on the sensor plane. The effective field of a bead influences the sensor, H_x is integrated over a general sensor area, A.

$$\langle H_x \rangle = \frac{1}{A}\int H_x dA \tag{13}$$

If the sensor geometry is considered as a circle, the effective field of a bead can be calculated from Eq. (13) as

$$\langle H_x \rangle = -\frac{M R^3}{3z_o^3}\frac{1}{(1 + \frac{\rho_s^2}{z_o^2})^{3/2}} \tag{14}$$

Here ρ_s is the radius of the circular ring sensor

And if the sensor geometry is quadrate the effective field is given by

$$\langle H_x \rangle = -\frac{M R^3}{3z_o^3}\frac{1}{(1 + \frac{\omega^2}{4z_o^2})(1 + \frac{\omega^2}{2z_o^2})^{1/2}} \tag{15}$$

here ω is the width of the cross-junction sensor

It is revealed from Eq. (14) and Eq. (15) that the field effect to the sensor is very much depending on the size of the sensor, , it is proportional to the invert cube of radius of circular sensor or of the width of a quadratic sensor ($\frac{1}{\rho^3}$ or $\frac{1}{\omega^3}$).

5.2. Biofunctionalization of the beads

It is known that the biotin-streptavidin is one of the strongest non-covalent biological interaction systems having a dissociation constant, 'K_d', in the order of 4×10^{-14} M leading to the strength and specificity of the interaction to be one of the most widely used affinity pairs in molecular, immunological and cellular assays [40]. Usually in most assays, streptavidin is coupled to a solid phase such as a magnetic bead, or a biosensor chip, while biotin is coupled to the biomarker of interest, often a nucleic acid or antibody. Taking advantages of magnetic labels and specific ligand-receptor interactions of the biomolecules one can manipulate, separate and detect specific biomolecules.
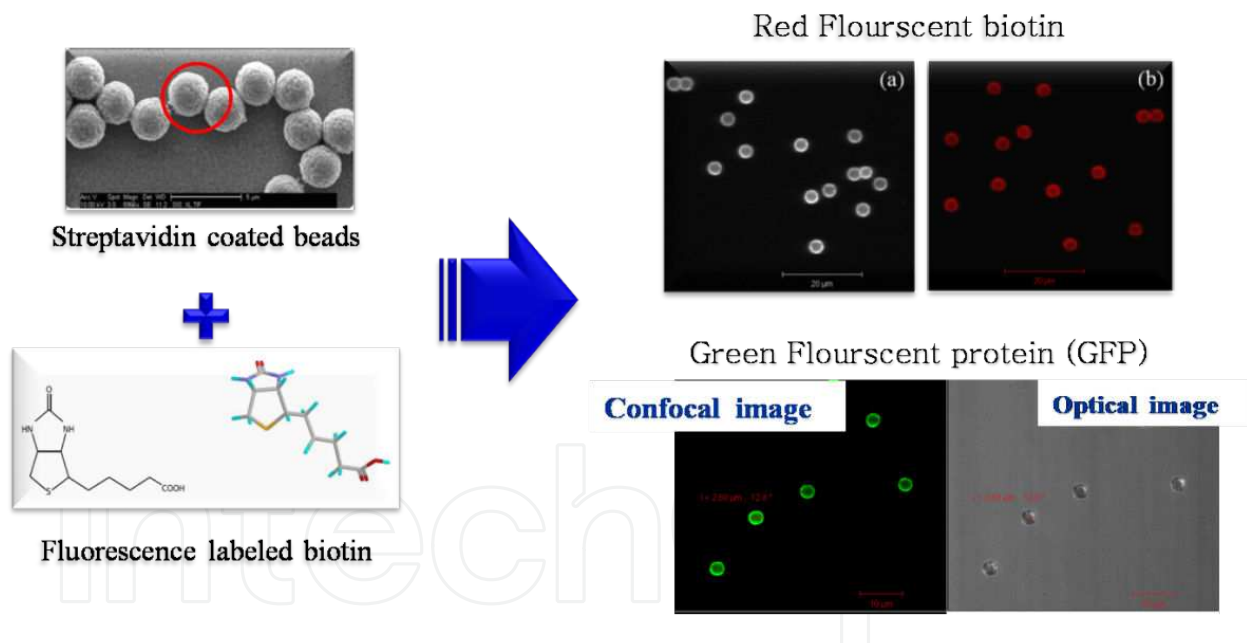
Figure 22. Procedure for the immobilization of fluorescent labeled biotin on the Streptavidin coated dynabeads measured by confocal optical microscope.

To demonstrate the translocation of streptavidin-biotin magnetic labels using the micro system, we have chosen the commercially available streptavidin coated magnetic beads (Dynabead® M-280) of 2.8 μm size to bind with fluorescent labelled biotin. Atto 520 is a new label with high molecular absorption (110.000) and quantum yield (0.90) as well as sufficient stokes shift (excitation maximum 520 nm, emission maximum 524 nm). Due to

an insignificant triplet formation rate it is well suited for single molecule detection applications. In this experiment, Atto 520 biotin is attached on the streptavidin coated magnetic beads and observed the fluorescence signal through confocal microscope. In order to attach the Atto 520 biotin on streptavidin coated magnetic labels, we have taken, 5 μl of streptavidin coated magnetic labels (Dynabead® M-280) mixed with 0.1 M PBS buffer solution (90 μl) with pH of 7, and 5 μl of fluorescent label biotin (chemical concentration of fluorescent label was 1 mg/200 μl in EtOH) also added to the previous mixing solution and continuously stirring the solution for 2 hours at room temperature for the reaction completion.

Fig. 22 provides the direct evidence of protein immobilization which was obtained by immobilizing green fluorescent protein (GFP) and observed the fluorescence through confocal laser microscopy.

5.3. Sensor size and bead detection capability

For the micro-bead detection using a PHE sensor, it is noted that the magnetization of the magnetic sphere is purely a dipole at the center of the sphere with a magnetic field at a distance identified by the dipole field from Eq. (15). The stray field of a single bead on the sensor surface could be crudely calculated by [41]

$$H_{\text{bead}} \approx -\frac{\chi V}{4\pi r^3} H \tag{16}$$

where V is the volume of magnetic bead, χ is the volume susceptibility of magnetic beads. This stray field is in the opposite direction to the applied field, thus it reduces the effective field on the sensor surface. Under the experiment conditions, the stray field of N beads on the sensor surface reduced the sensor output signal as follows:

$$V_{\text{bead}} = V_{\text{PHR}}(H_{\text{eff}}) \approx V_{\text{PHR}}(1 - NH_{\text{bead}}) \approx V_{\text{PHR}} + \Delta V_{\text{bead}} \tag{17}$$

where H_{eff} is the effective field on the sensor surface, S is the sensor sensitivity of PHR sensor. The voltage signal, ΔV_{bead} generated by the magnetic bead themselves can be expressed as

$$\Delta V_{\text{bead}} = V_{\text{bead}} - V_{\text{PHR}} \approx V_{\text{PHR}}\left(\frac{N\chi V}{4\pi r^3} H\right) \tag{18}$$

By substituting the value $\chi = 0.13$ [39] and $r = 1.55$ µm (the distance including the radius of Dynabeads® M-280 and the thickness of passivated SiO and Ta layers) into Eq. (17), the stray field of single bead is estimated to be $H_{\text{bead}} \sim 0.03\, H$ under the applied field. The number of bead separately placed on the sensor surface can be calculated using the PHR sensor.

Fig. 23 shows the V_{PHR} and the V_{bead} in the functions of magnetic field with number of bead N=1, 5, and 10, respectively. It is clearly shown that the beads on the sensor surface modify the PHR signal due to the small stray field compared with applied magnetic field.

In the PHR sensor, the V_{PHR} can be used the reference signal. The difference voltage ΔV_{bead} between the V_{PHR} and V_{bead} can be estimated, which is shown in Fig. 24.

The pure bead signal ΔV_{bead} is small compared with V_{PHR}. However, the ΔV_{bead} changes with the applied magnetic field and show maximum and minimum values at special magnetic field, which is due to the PHR sensor performance. Therefore, the bead detection capability can be determined at the maximum and minimum ΔV_{bead}. If we set the applied field at the maximum or minimum value of ΔV_{bead}, we can detect the magnetic bead with high signal voltage.
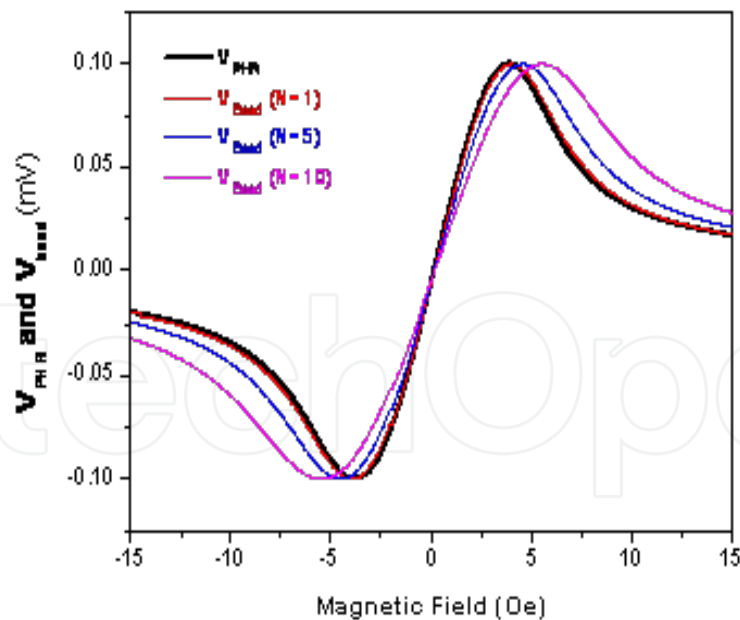
Figure 23. V_{PHR} without bead (black solid line) and V_{bead} with bead (N=1, 5 and 10) by using the F/AF bilayers in the functions of applied magnetic field H.
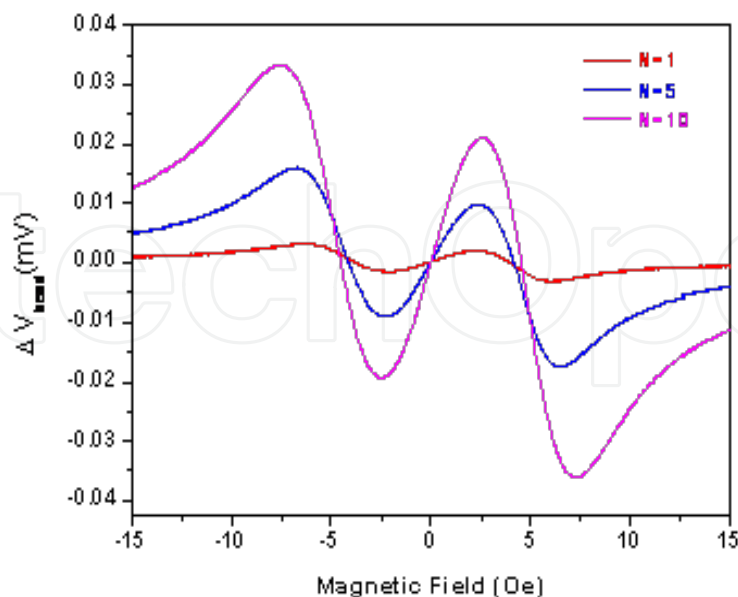
Figure 24. Calculation of ΔV_{bead} of the PHR sensor with N=1, 5 and 10.

5.3.1. Multi-bead detection

We performed the magnetic bead detection using PHR sensor using Ta(3)/NiFe(16)/Cu(1.2)/ NiFe(2)/IrMn(10)/Ta(3) (nm) to demonstrate the feasibility of magnetic bead detection for bio applications. The diluted 0.1 % magnetic bead solution streptavidin coated Dynabeads® M-280 is used for bead drop and wash experiments on the sensor surface. The real-time pro‐ file measurements of the PHE voltage for magnetic bead detection are carried out in the op‐ timum conditions, that is, in an applied magnetic field of 7 Oe and with a sensing current of 1 mA. The results are illustrated in Fig. 25 for three consecutive cycles. The lower state rep‐ resents the signal change in sensor output voltage after dropping the magnetic bead solution on the sensor surface whereas the higher state represents the sensor output voltage after washing magnetic beads from the sensor surface. Total output signal annuls in three consec‐ utive cycles were found to be about 7.1 μV, 16 μV and 21.8μV for the first step and 11.3 μV and 16.7 μV in the second step of the second and third cycles, respectively. It is clearly shown from the figure that for the first cycle, the signal changed by one-step and the signal was further changed into two steps in the second and third cycles.

This two step-type profile is due to the aggregation process of the magnetic beads on the sensor surface. The aggregation of the magnetic beads occurs at the drying stage. That is, after dropping the bead solution on the sensor surface, it needs some time to dry. The first step changes of the signals are assumed to be due to the viscous flow motion for stabiliza‐ tion as well as the Brownian motion of the beads. When the solution dries, the beads rear‐ range. During this time, some beads aggregate and become clusters on the sensor surface.
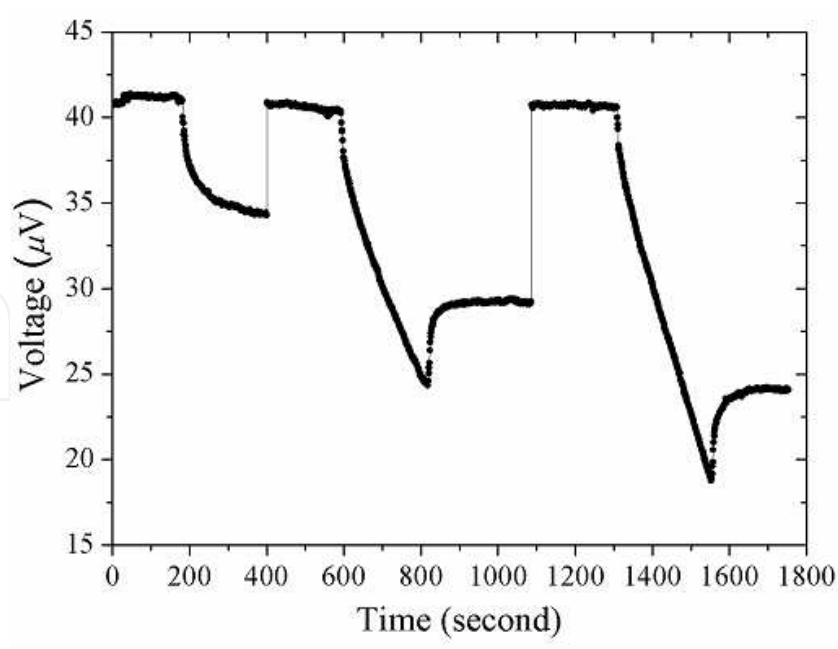
Figure 25. Real-time profile of PHR sensor under an applied magnetic field of 7 Oe with the sensing current of 1 mA

This lessens the total stray field on the sensor surface and hence, the second step in the second and third cycles was observed in the real-time profile.

In the process of analyzing the micro-bead detection using PHE sensor, it is noted that the direction of magnetic field H and the stray field of magnetic bead on the sensor surface H_{bea}d (Eq. (16)) are oppositely aligned, and thus the effective field on the sensor surface is reduced.

Thus, a rough estimate of the number of magnetic particles on the sensor surface in this identical experiment based on the reduced stray field and sensor output signal can be expressed from Eq. (18) by rephrasing it again here for better clarity:

$$\Delta V_{bead} = V_{PHR}\left(\frac{N\chi V}{4\pi r^3}H\right)$$

By substituting the value $\chi = 0.13$ and $r = 1.55$ μm (the distance including the radius of Dynabeads® M-280 and the thickness of passivated SiO_2 and Ta layers) into Eq. (16), the stray field of single bead is estimated to be 2.2×10^{-2} Oe under the applied field of 7 Oe. Theoretically, with the sensor sensitivity $S = 7.6$ μV/Oe and the sensing current $I = 1$ mA, the number of beads separately placed on the sensor surface can be calculated in the first step of the three cycles by using Eq. (18), which are estimated to be about 4, 10 and 13 beads, respectively.

These estimated results strengthen our explanation. It is clearly shown in the first cycle, the number of beads on the sensor surface is estimated to be small, and the distance among beads on the sensor junction is far enough to avoid the effect from the rearrangement of beads during the drying stage. In the second and third cycles, the number of magnetic beads

on the sensor junction is larger; they easily aggregate to become clusters under applied magnetic field due to short bead-bead distance

5.3.2. Single bead detection

We performed single magnetic bead detection experiments on several kinds of sensor structures such as spin-valve and bilayer exchange biased thin films [27, 42 - 44], and the representative results are being presented here. For the purpose of performing single micro-bead detection, the PHR sensor with the junction size of 3 μm × 3 μm was fabricated using Ta(5)/NiFe(16)/Cu(1.2)/NiFe(2)/IrMn(15)/Ta(5) (nm). This is the optimized spin-valve thin film for the PHR sensor in our lab. A droplet of 0.1 % dilute solution of the Dynabeads® M-280 was introduced on the surface of the sensor. A single micro-bead was isolated and positioned on the center of the sensor junction by using a micro magnetic needle which is known as a tweezer method. The magnetic needle was prepared by using a soft magnetic micro wire, the wire is magnetized by attaching a permanent magnet to one end of the wire, the single magnetic bead is attracted with the other end due to the magnetic field of the wire and it is dragged and positioned to the center of the sensor junction. It is noteworthy that the magnetic bead is attracted by the magnetic force; this force is strong enough to compensate the Brownian motion during the experiment. The experiment was carried out under the observation of an optical microscope. When the solution dried, the bead was fixed on to the sensor surface.

Since the magnetic properties of the MR as well as the PHE response to the magnetic field are described in the previous section, the results of single bead detection using 3 μm × 3 μm PHR sensor will be discussed here.

The SEM image of a single bead on the center of the sensor junction is shown in the Fig. 26(a). The voltage profiles of the PHE sensor in the absence and presence of a single micro-bead are presented in Fig. 26(b) by black circle and red rectangle ones, respectively. It is shown from the figure that in the increasing region of the PHE voltage profile (in the field ranging from 0 Oe to 10.6 Oe), the $V_{\text{PHE}}(H)$ is decreased when the magnetic bead exists on the sensor surface and vice versa for the decreasing region of the PHE voltage profile (at the fields exceeding 10.6 Oe).

For understanding the role of a single micro-bead detection using a PHE sensor, we consider the voltage drop by stray field of a single magnetic bead. The calculation method is the same as deduced for Eq. (18). And when considering that the magnetic bead is located on the center of sensor junction, the stray field affects the PHE voltage as follows:

$$V_{\text{stray}} = I \times S \times \left(1 - k\frac{\chi V_{\text{bead}}}{4\pi z^3}\right) \times H_{\text{app}} \tag{19}$$

where V_{stray} denotes the voltage change due to the stray field of magnetic bead, $S = \dfrac{\partial V_{\text{PHE}}}{\partial H}$ is the sensitivity of the sensor at instantaneous applied fields.
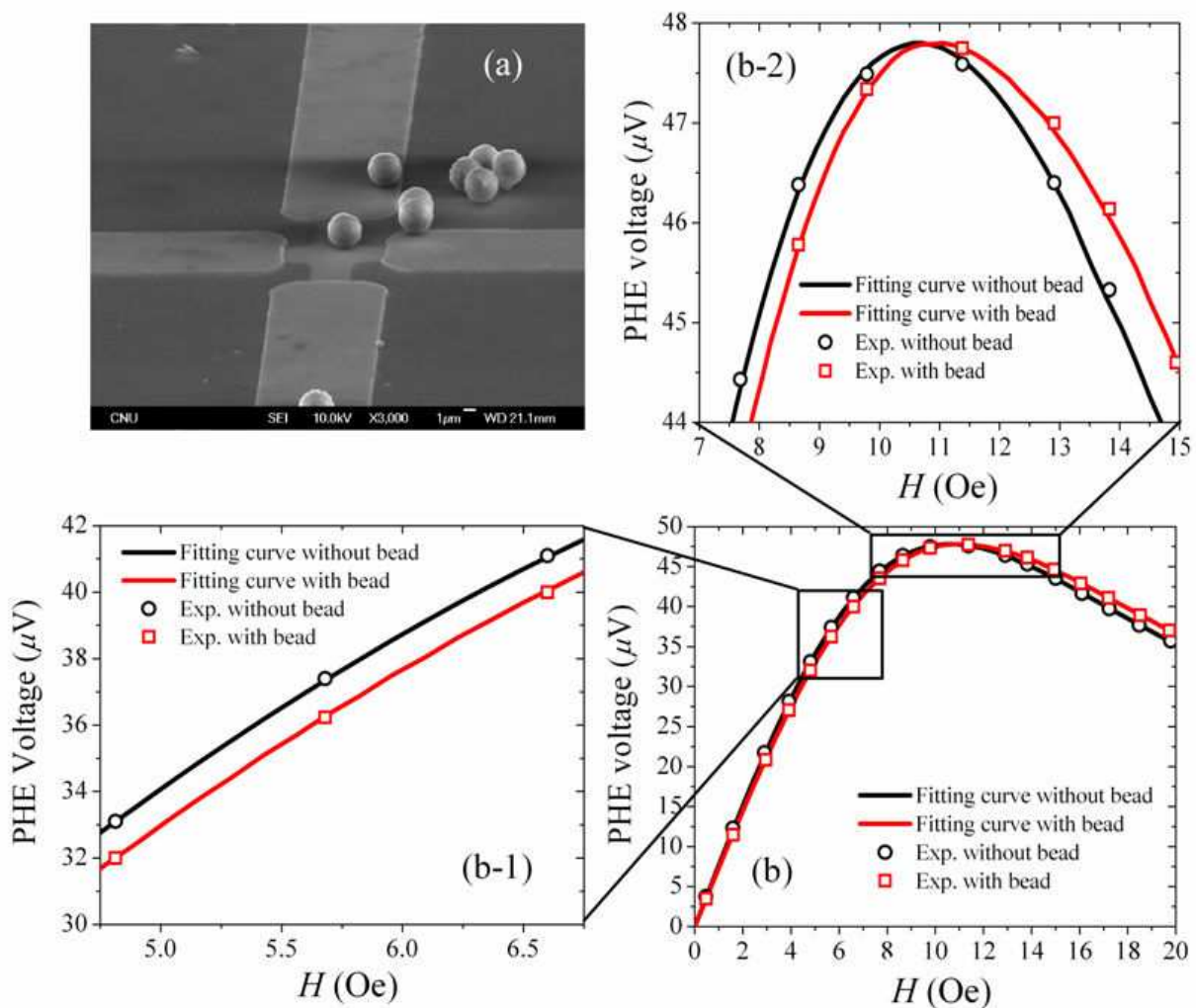
Figure 26. (a) The SEM image of the sensor junction in the presence of a single micro-bead, (b) the theoretical and experimental PHE voltage profiles in the absence and presence of a micro-bead, (b-1) enlarged picture of the increasing PHE voltage region at the field range of 4.75-6.74 Oe and (b-2) enlarged picture of the PHE voltage profiles around the maximum PHE voltages [44].

By substituting $\chi = 0.13$ [39] in Eq. (19) with active fraction of $k = 0.62$ and $z = 1.55$ μm (along with 150 nm thick SiO_2 passivation layer and 1.4 μm of magnetic bead radius), the PHE voltage is calculated at instant applied fields for the presence of a micro-bead. The solid lines in the Fig. 26(b) illustrate the calculated profiles for the case of absence and presence of a micro-bead, respectively. These calculated results are in good agreement with the experimental results.

By comparing the PHE voltage profiles in the absence and presence of a micro-bead, one can find that (*i*) at low magnetic fields, the PHE voltage increases with the field increase, *i.e.* the sensitivity of the sensor is positive. In this case, the presence of magnetic bead lessens its PHE voltage as illustrated in Fig. 26(b-1). (*ii*) In the presence of the magnetic bead, the maximum PHE voltage shifts to a higher field with an amount of H_{bead} as presented in Eq. (16); at
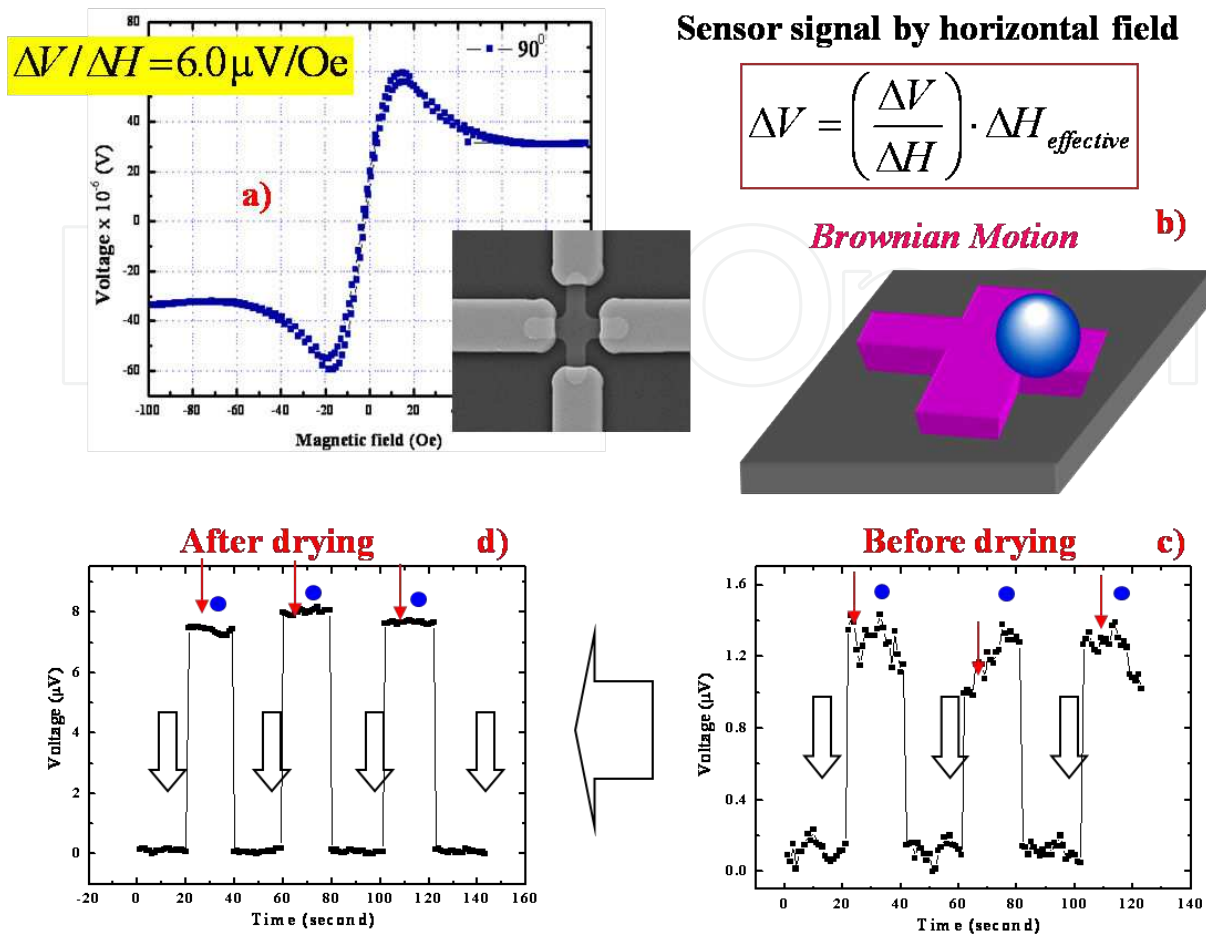
Figure 27. Voltage change of the PHR sensor versus applied field when a single magnetic bead appear on the sensor surface.

about 10 Oe this stray field strength is approximately 0.43 Oe. (*iii*) At higher applied fields (> 10 Oe), the PHE voltage decreases with the field increase, *i.e.* the sensitivity of the sensor is negative. In this case, the presence of magnetic bead increases the PHE voltage with an amount of $k \dfrac{\chi V_{\text{bead}}}{4\pi z^3} I \cdot S \cdot H_{\text{app}}$. This is clearly evident in the Fig. 26(b-2) and thus the PHE signal satisfies Eq. (19).

In particular, at low field range, a very good linear and large change of the PHE voltage always occur, so this field range is usually chosen to demonstrate the feasibility of the digital detection of the magnetic beads [10-14]. In our approach for this sensor, the signal change versus the applied field is extracted from PHE voltage curves in the presence and absence of magnetic bead, the result is drawn in Fig. 27, the maximum change of $V_{\text{PHE}}(H)$ about 1.14 μV can be obtained at the applied field ~ 5.6 Oe. This calculated result satisfies Eq. (19). Further, Fig 26(b) shows that there is a very good agreement between the single bead measurement data and the theoretical curves. There is only a very small noise scatter of experiment data from the fitting curve, this is the evidence showing that the fabricated PHE sensor has high

SNR. Therefore, the PHE sensor has advantages for more accurate detection of the small stray fields of magnetic beads.

This simple calculation is suitable for the effect of a single bead on the center of small size sensor junction. When the area of the sensor junction is larger than the area of magnetic beads, the calculation must be considered the effect of the magnetic bead from different positions of sensor junction and the contribution of nearby beads or chains of beads on the sensor. In such a case the output signal changes negative for the bead inside of the sensor junction and changes positive for the beads outside of the junction. Moreover, the signal change does not depend on the number of magnetic beads proportionally. This was studied systematically and was reported by P.P. Freitas *et al.*,[23], L. Ejsing et al., [9] and Damsgaard *et al.*, [45].

### 5.4. Integration of magnetic sensors/microfluidic channels

In this part, we design and optimize the planar Hall ring sensor for detecting the hydrodynamic magnetic labels. Once the magnetic labels appear on one arm of the ring sensor, the resistance of the sensor will be changed, the role of resistance change obey the Wheatstone bridge circuit geometry hence the sensor is very sensitive to detect the magnetic labels.

Planar Hall ring sensor was fabricated by photolithography technique. Sensor material Ta(3)/NiFe(10)/IrMn(10)/Ta(3) (nm) was fabricated by using a DC sputtering system with the based pressure of 7×10^{-8} Torr. The field sensitivity of the ring sensor based on the bilayer thin film was found to be about 0.3 mV.Oe^{-1}. The sensor was integrated with a microfluidic channel, which can produce the laminar flow of the magnetic labels (beads and/or tags) in the specific arms of the ring sensor by hydrodynamic flow focusing technique. This magnetic platform can detect even a single magnetic bead of 2.8 μm motion in real time by the measurement system with a sampling rate of 5 kHz.

The schematic representing the integrated magnetic platform is shown in Fig. 28. In magnetic bead separation experiments initially the magnetic beads with different sizes are injected into the main stream of the microfluidic channel with certain fluidic flow rate. Then the beads are gathered at the weir in the fluid channel and then sorted according to the attractive force exerted on the magnetic bead by the magnetic elements/magnetic pathways. Therefore, the labeled magnetic beads of same kind will attract to one of the magnetic pathways in the sub channel. The weir at the entrance of the sub-channels opposes the beads temporarily for magnetic beads whose magnetization is insufficient to be attracted by the magnetic elements. But, the beads whose magnetization is sufficient to be attracted by the poles of the saturated ellipses due to the external rotating magnetic field can overcome the weir.

After successful separation of the magnetic beads of different sizes we wish to adopt two types of different sensing techniques such as an array of PHR biosensors and multi-segmented nanowires. The planar array of PHR sensor can detect magnetic beads with micron size only. But in case of nanometer size magnetic beads, we wish to use simple read out

technique of multi-segmented nanowires. We are also planning to combine magnetic pathway method with the microwire and coil method.
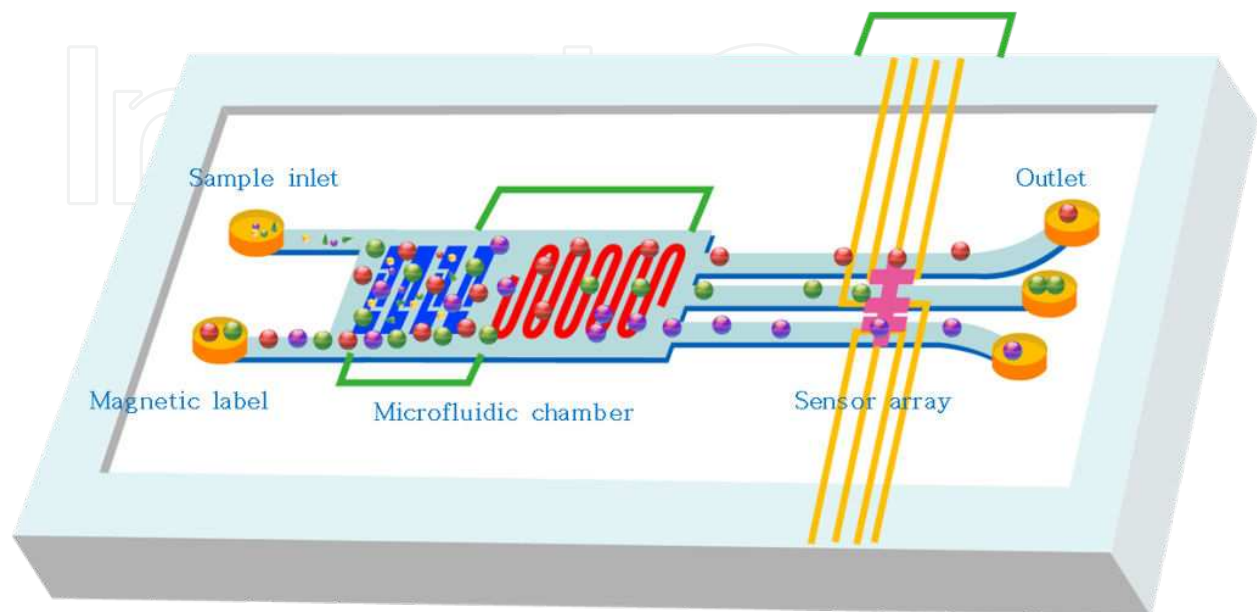
Figure 28. Schematic represents the magnetic platform integrating an array of planar Hall ring sensors and a microfluidic channel.

6. Conclusions

The underlying principle for magnetic biosensing has been elaborately described at first with the examples of different magnetoresistive sensing techniques. Then, the planar Hall resistance sensor has been shown as one of the best sensors for conducting magnetic bead detection experiments. While making an in depth study on the capabilities of a PHR sensor in different configurations and geometries, the sequence of narration ultimately has lead towards describing the evolution of hybrid AMR and PHR ring sensor in spin-valve configuration with optimized performance for precise detection of even single magnetic bead. Biofunctionalization experiments were also conducted to ensure that our PHR sensor is capable of biomolecule recognition. Therefore, our present sensor can be used to promote for the biomolecular recognition and other molecular interaction detection. This novel planar Hall effect based sensor has been further demonstrated that it can be easily integrated into a lab-on-a-chip and is feasible for bead detection in the sensing current generated magnetic field (without the external applied magnetic field) so as to ensure it an efficient tool for high sensitive biomolecules recognition.

Author details

Tran Quang Hung[1,4], Dong Young Kim[2], B. Parvatheeswara Rao[3] and CheolGi Kim[1*]

*Address all correspondence to: cgkim@cnu.ac.kr

1 Department of Materials Science and Engineering, Chungnam National National University, Daejeon, Korea

2 Department of Physics, Andong National University, Andong, Korea

3 Department of Physics, Andhra University, Visakhapatnam, India

4 Laboratoire Charles Coulomb, CNRS-University Montpellier 2, Montpellier, France

References

[1]   M.M. Miller, G.A. Prinz, S.F. Cheng, S. Bounnak, Appl. Phys. Lett. 81, 2211–2213 (2002).

[2]   . Andreev, P. Dimitrova, Journal of Optoelectronics and Advanced Materials 7, 199-206 (2005).

[3]   D.R. Baselt, G.U. Lee, M. Natesan, S.W. Metzger, P.E. Sheehan, R.J. Colton, Biosens. Bioelectron. 13, 731–739 (1998).

[4]   D.K. Wood, K.K. Ni, D.R. Schmidt, A.N. Cleland, Sensors and Actuators A 120, 1–6 (2005).

[5]   .C. Rife, M.M. Miller, P.E. Sheehan, C.R. Tamanaha, M. Tondra, L.J. Whitmana, Sensors and Actuators A 107, 209–218 (2003).

[6]   . Schotter, M. Panhorst, M. Brzeska, P. B. Kamp, A. Becker, A. Pühler, G. Reiss, H. Brueckl, Nanoscale Devices - Fundamentals and Applications, edited by R. Gross et al.(Springer) 35–46 (2006). GMR-TMR

[7]   .S. Moodera, L.R. Kinder, T.M. Wong, R. Meservey, Phys. Rev. Lett. 74, 3273 (1995).

[8]   P.A. Besse, G. Boero, M. Demierre, V. Pott, R. Popovic, Appl. Phys. Lett. 80, 4199–4201(2002).

[9]   L. Ejsing, M. F. Hansen, A. K. Menon, H. A. Ferreira, D. L. Graham and P. P. Freitas, Appl. Phys. Letts. 84, 4729 (2004).

[10] N.T. Thanh, K.W. Kim, C.O. Kim, K.H. Shin, and C.G. Kim, J. Magn. Magn. Mater. 316, e238 (2007).

[11] N. T. Thanh, L. T. Tu, N. D. Ha, C. O. Kim, CheolGi Kim, K.H. Shin, and B. Parva-theeswara Rao, J. Appl. Phys. 101, 053702 (2007).

[12] P. P. Freitas, H. A. Ferreira, D. L. Graham, L. A. Clarke, M. D. Amaral, V. Martins, L. Fonseca, J. S. Cabral, in Magnetoelectronics, edited by M. Johnson (Elsevier, Amsterdam, 2004) and references therein.

[13] (a) B. D. Tu, L. V. Cuong, T. Q. Hung, D. T. H. Giang, T. M. Danh, N. H. Duc, C. G. Kim, IEEE Trans. Magn. 45, 2378 (2009); b) T. Q. Hung, S. J. Oh, B. D. Tu, N. H. Duc, L. V. Phong, J.-R. Jeong, and C. G. Kim, IEEE Trans. Magn. 45, 2374 (2009).

[14] E. Ejsing, the dissertation of doctor of philosophy, Technical University of Denmark, Denmark (2003).

[15] a) F. Nguyen Van Dau, A. Schuhl, J.R. Childress, M. Sussiau, Sensors and Actuators A, 53, 256-260 (1996); b) N. T. Thanh, B. Parvatheeswara Rao, N. H. Duc, and CheolGi Kim, phys. stat. sol. (a) 204, 4053–4057 (2007).

[16] T. R. Mcguire and R. I. Potter, "Anisotropic magnetoresistance in ferromagnetic 3d alloys," IEEE Trans. Magn. 11, 1018-1038 (1975).

[17] B. Dieny, J. Magn. Magn. Mater. 136, 335 (1994).

[18] S. S. Parkin, C. Kaiser, A. Panchula, P. M. Rice, B. Hughes, M. Samant and S. H. Yang, "Giant tunneling magnetoresistance at room temperature with MgO (100) tunnel barriers," Nature Mat., 3, 862-867 (2004).

[19] S. Yuasa, T. Nagahama, A. Fukushima, Y. Suzuki, and K. Ando, "Giant room temperature magnetoresistance in single crystal Fe/MgO/Fe magnetic tunnel barriers," Nature Mat., 3, 868-871, (2004).

[20] S. J. Oh, Le Tuan Tu, G. W. Kim, and CheolGi Kim, Phys. Stat. Sol. (a) 204, 4075 (2007).

[21] G. H. Yu, M. H. Li, F. W. Zhu, H. W. Jiang, W. Y. Lai, and C. L. Chai, Appl. Phys. Lett. 82, 94 (2003).

[22] T. Lucinski, G. Reiss, N. Mattern, and L. van Loyen, J. Magn. Magn. Matter. 189, 39 (1998).

[23] P. P. Freitas, R. Ferreira, S. Cardoso, and F. Cardoso, J. Phys.: Condens. Matter. 19, 165221 (2007).

[24] C. Parados, D. Garcia, F. Lesmes, J. J. Freijo, and A. Hernando, Appl. Phys. Lett. 67, 31 (1995)

[25] D. Y. Kim, C. G. Kim, B. S. Park, C. M. Park, "Thickness dependence of planar Hall resistance and field sensitivity in NiO(30 nm)/NiFe(t) bilayers" J. Magn. Magn. Mater. 215-216, 585–588 (2000).

[26] (a) www.ssec.honeywell.com; b) Candid Reig, Marıa-Dolores, Cubells-Beltran and Diego Ramirez Munoz, sensors. 2009, 9, 7919 – 7942; c) Hoffmann, K., Applying the Wheatstone bridge circuit, HBM S1569-1.1en, HBM, Darmstadt, Germany.

[27] N.T.Thanh, the dissertation of doctor of philosophy, Chungnam National University, Korea (2006)

[28] (a) W. H Meiklejohn; C. P Bean, Physical Review, 105, 904–913 (1957); (b) J. Nogués, Ivan K. Schuller, J. Magn. Magn. Mater., 192, 203 (1999).

[29] (a) William C. Cain and Mark H. Kryder, IEEE Trans. Magn. 25, 2787 (1989); b) Z. Q. Lu, G. Pan, and W. Y. Lai, J. Appl. Phys. 90, 1414 (2001).

[30] B. Dieny, V. S. Speriosu, S. Metin, S. S. P. Parkin, B. A. Gurney, P. Baumgart, and D. R. Wilhoit, J. Appl. Phys. 69, 4774 (1991).

[31] N. J. Gökemeijer, T. Ambrose, and C. L. Chien, Phys. Rev. Lett. 79, 4270 (1997).

[32] T.Q. Hung, Sunjong Oh, Brajalal Sinha, J.R. Jeong, Dong-Young Kim and CheolGi Kim, J. Appl. Phys. 107, 09E715 (2010).

[33] B. Dieny, J. Phys.: Condens. Matter. 4, 8009 (1992).

[34] B. Dieny in: Magnetoelectronics, Ed. M. Johnson, (Elsevier, Amsterdam 2004).

[35] T. Q. Hung, J.-R.Jeong, D.Y. Kim, N. H. Duc and C. G. Kim, J. Phys. D: Appl. Phys., 42, 055007.1-5 (2009).

[36] M. Li, S.-H. Liao, C. Horng, Y. Zheng, R. Y. Tong, K. Ju, and B. Dieny, IEEE Trans. Magn., 37, 1733 (2001).

[37] D. Y. Kim, B. S. Park and C. G. Kim, J. Appl. Phys. 88, 3490 (2000).

[38] Sunjong Oh, P.B. Patil, T.Q. Hung, B. Lim, M. Takahashi, Dong Young Kim and CheolGi Kim, Solid State Commn., 151, 1248-1251 (2011).

[39] See physical characteristics of Dynabeads® M-280 streptavidin at http://tools.invitro-gen.com/content/sfs/manuals/112.05D06D%20602.10%20Dynabeads %20M280%20Streptavidin%20(rev%20012).pdf

[40] Anders Holmberg, Anna Blomstergren, Olof Nord, Morten Lukacs, Joakim Lunde-berg and Mathias Uhlén, Electrophoresis, 26, 501–510 (2005).

[41] L. Ejing, M. F. Hansen, and A. K. Menon, "Planar Hall effect magnetic sensor for mi-cro-bead detection," in Conf. Proc., Eurosensors 2003, 1095–1098 (2003).

[42] Bui Dinh Tu, Tran Quang Hung, Nguyen Trung Thanh, Tran Mau Danh, Nguyen Huu Duc and CheolGi Kim, J. Appl. Phys. 104, 074701 (2008).

[43] Tran Quang Hung, the dissertation of doctor of philosophy, Chungnam National University, Korea (2010).

[44] (a) Tran Quang Hung, Sunjong Oh, Jong-Ryul Jeong, and CheolGi Kim, Sensors and Actuators A, 157, 42–46 (2010); b) Brajalal Sinha, S. Anandakumar, Sunjong Oh, CheolGi Kim, Actuators A, 182, 34–40 (2012).

[45] C.D. Damsgaard and M.F. Hansen, J Appl. Phys. 103, 064512 (2008).